Petrogenesis of late-Variscan high-K alkali-calcic granitoids and calc-alkalic lamprophyres: The Aber-Ildut/North-Ouessant complex, Armorican massif, France

Martial Caroff, Cyrill Labry, Bernard Le Gall, Christine Authemayou, Denise Bussien Grosjean, Marcel Guillong

Petrogenesis of late-Variscan high-K alkali-calcic granitoids and calc-alkalic lamprophyres: the Aber-Ildut/North-Ouessant complex, Armorican massif, France

Martial Caroff [a,*], Cyrill Labry [a], Bernard Le Gall [a], Christine Authemayou [a], Denise Bussien Grosjean [a,1], Marcel Guillong [b]

[a] UMR/CNRS n°6538 « Domaines Océaniques », Institut Universitaire Européen de la Mer, Université de Brest, Place Nicolas Copernic, 29280 Plouzané, France

[b] Institute of Geochemistry and Petrology, Department of Earth Sciences, ETH Zurich, Clausiusstrasse 25, 8092 Zurich, Switzerland

* Corresponding author: caroff@univ-brest.fr

[1] Present address : Musée cantonal de Géologie, Quartier UNIL-Dorigny, Bâtiment Anthropole, 1015 Lausanne, Switzerland.

Keywords: Leucogranite; Calc-alkaline lamprophyre; Minette; Tetrad effect; Variscan belt; Armorican Massif

Abstract

The Aber-Ildut/North-Ouessant Variscan granitoid complex in the Armorican Massif is an example of high-K alkali-calcic zoned pluton, c. 304 Ma in age. A first magmatic batch intruded through a northern EW-trending sinistral transcurrent shear zone, before injecting southwards as a huge horizontal zoned sill, with moderately peraluminous muscovite-free granitoids in the north and strongly peraluminous muscovite-bearing leucogranites to the south. The second magmatic stage resulted in the intrusion of a large two-mica leucogranitic body from a root zone along the same shear zone, prior to the end of crystallization of the first injection. Finally, ultrapotassic dykes, including calc-alkalic lamprophyres (leucominettes), intrude the complex. The strongly peraluminous granites are interpreted as pure melting products of crustal clay-rich pelitic material. All the other petrographic types, including leucominettes, are thought to result from mixing of crustal melts and mantle-derived mafic liquids. Highly silicic tourmaline-bearing leucogranites are significantly affected by a tetrad effect, in relation with REE complexing behavior. Aber-Ildut/North-Ouessant granitoids probably formed during the Variscan late-orogenic stage associated with exhumation and lithospheric thinning, at low pressure and by advective heating of a $\leq$ 50 km-thick crust from hot metasomatized asthenosphere.

1. Introduction

High-K alkali-calcic – and calc-alkalic – granitoids are distinctive in their high potassium content and their lack of iron enrichment (Frost et al., 2001). Although many of

them are metaluminous, the most siliceous terms are peraluminous (aluminium saturation index > 1). Peraluminous granitoids are mainly divided into S-type granites (Chappell and White, 1974) and muscovite-leucogranites (Barbarin, 1999), two types clearly distinguished on the basis of major elements by Patiño Douce (1999). Following this author, muscovite-leucogranites are pure crustal melt, which is not the case for the S-type granitoids. Sylvester (1998) proposed a supplemental category, with the individualization of strongly peraluminous (SP) granites, when the aluminium saturation index is higher than 1.1.

Strongly peraluminous (SP) granites occur generally as isolated plutons within overthickened crust in high pressure collision chains (Alps, Himalaya), and in association with high-K calc-alkalic/alkali-calcic granitoids within ≤ 50km-thick crust in high temperature chains (Variscides, Lachlan). Both granitoid types are commonly referred to as late- or post-orogenic magmatism (Maniar and Piccoli, 1989; Sylvester, 1998; Barbarin, 1999; Frost et al., 2001).

The Aber-Ildut/North-Ouessant granitoid complex (hereafter referred to as AI-NO) belongs to a set of Variscan high-K plutons, c. 300 Ma in age, all located along the northern coast of the Armorican massif (Chauris, 1994). Although divided into three submassifs, the complex constitutes a coherent structure, rooted in a sinistral NE/SW-trending shear zone. The three most remarkable features are: (1) the presence of a large spectrum of petrologic varieties, ranging from quartz monzodiorites to tourmaline leucogranites and leucominettes; (2) the fact that each unit sets up prior to the end of crystallization of that emplaced just before: except for two petrographic types (late microgranitic and microsyenitic dykes), there is on the field either a progressive transition from one unit to another or mingling relations between them; and (3) the coexistence in a single pluton of high-K alkali-calcic moderately peraluminous (MP) granitoids with contemporaneous both strongly peraluminous (SP) leucogranites and calc-alkalic lamprophyres.

In this paper, a new set of geochronological, petrologic and geochemical data is presented to discuss the conditions of unit emplacements, the petrogenetic connection between the various granitic/lamprophyric magmas and, lastly, a source model with respect to the late orogenic Armorican context.

2. Analytical techniques

2.1. U/Pb zircon dating

Zircon grains were extracted by standard mineral separation and placed in epoxy resin. In order to avoid perturbed zones and inherited cores, the grains were polished to their equatorial plane, and then imaged by cathodoluminescence (CL; CamScan MV2300, Earth Sciences Institute, University of Lausanne, Switzerland).

Dating was performed by laser ablation (LA) inductively coupled plasma mass spectrometry (ICP-MS) at the Institute of Geochemistry and Petrology (ETH, Zurich, Switzerland), combining a Resonetics Resolution 155 excimer laser (ArF, 193 nm) to a Thermo Element XR magnetic sector mass spectrometer. Laser beam diameter of 30 microns and fluence of c. 2 J/cm^2 at a frequency of 5 Hz were used. After surface cleaning and wash out, the reading composed of c. 10 seconds of gas blank and 40 seconds of ablation signal started. Ablated material was carried by He flux (0.6 - 0.7 l/min) and sample gas (0.8 - 1.1 l/min) was homogenized by a Squid system.

A run of several unknowns was framed by analyses of GJ-1 as internal standard and of three natural zircons (Temora, Plešovice and 91500) to monitor the external reproducibility. Raw data were processed using Glitter software package (van Achtenberg et al., 2001), and the Concordia age and diagram were obtained by Isoplot/Ex v. 4.15 (Ludwig, 2008). Repeated

measurements on the GJ-1 gave an age of 602.0 ± 2.7 Ma (2 sigma, n = 14) and the Plešovice resultant age is 338.3 ± 2.2 Ma (2 sigma, n = 4), which is within error in the range of the certified value (337.13 ± 0.37 Ma, Sláma et al. 2008).

Zircon grains extracted from the porphyritic monzogranite 13DB05 (see the following section for the nomenclature) are pinkish, mostly of gem-quality, with few inclusions. They are prismatic, elongated (2:1) and can reach length up to 250 microns. CL images reveal nice oscillatory magmatic domains, sometimes convolute zones, with frequent inherited cores that can be easily determined. Even with a careful selection of grains, most of the dating analyses are not concordant and were thus disregarded (90% of our analyses). Roughly, half of these discordant ages shows clearly mixing with inherited fraction, and the second half with discordant young ages is affected by lead loss. For very few grains, the discordancy is so high that it is more probably linked to analytical problems with the ^{207}Pb detection.

2.2. Mineral and whole-rock analyses

Mineral compositions were determined using a Cameca SX-100 electron microprobe (Microsonde Ouest, Brest, France) with an acceleration voltage of 15kV, a beam current of 2nA and a beam diameter of 1 µm.

To get representative geochemical whole-rock analyses, at least 400 g of material for fine-grained samples and 800 g for coarse-grained samples were prepared. A statistical method of alternate shoveling was applied in view to homogenize the coarse gravel after a first grinding (Pitard, 1993).

Whole-rock major and trace elements and isotopic ratios were determined at the PSO/IUEM (Pôle Spectrométrie Océan, Institut Universitaire Européen de la Mer, Brest, France). Major elements were analyzed by inductively coupled plasma-atomic emission

spectrometry (ICP-AES) using a Horiba Jobin Yvon® Ultima 2 spectrometer and following the analytical procedure of Cotten et al. (1995). They were determined from an H_3BO_3 solution, boron being used as an internal standard. Relative standard deviations are < 2% (< 1% for SiO_2), except for low values (< 0.50 wt%), for which the absolute standard deviation is ± 0.01 wt%. Trace elements were determined by high-resolution ICP-MS, using a Thermo Element 2 spectrometer, following the sample preparation and analytical procedure described by Barrat et al. (1996, 2000), who have developed a routine method using an ion-exchange chromatography procedure. Aliquots of the mother solutions were spiked with a solution of pure Tm and then evaporated to dryness. Relative standard deviations are < 5% for most of trace elements and < 10% for Nb, Gd, Tb, Ta, Ni, Zn and Rb. Because of zircon resistance against dissolution, a second method was tested to improve Zr and Hf concentrations in some granitic samples. Thus, seven zircon-bearing samples were analyzed a second time by using high pressure Teflon vessel bombs, in association with $HClO_4$, following the sample preparation of Révillon and Hureau-Mazaudier (2009). However, this method was not selected, as leading to erratic results for the rare earth elements, without any significant changes in mean concentrations. Consequently, the Zr and Hf data presented here have to be considered with caution and are not shown in any diagram.

Sr isotopic ratios were measured by thermal ionization mass spectrometry (TIMS), while Nd isotopic ratios were determined using a multicollector ICP-MS (PSO/IFREMER, Brest, France). The protocol for element separation is described in Richard et al. (1976) and White and Patchett (1984).

3. Geology

3.1. Regional context

The Late Variscan development of the Armorican orogenic belt is dominated by large-scale strike-slip tectonics, coeval to 308-300 Ma-old synkinematic granitic intrusions along two ductile shear zones: the South Armorican dextral Shear Zone (Berthé et al., 1979), and the Plouguerneau-Guisseny sinistral Shear Zone (PGSZ), in the Leon Domain (Chauris, 1994). In the latter area, the Aber-Ildut/North-Ouessant complex roots to the north along the steeply-dipping and NE-/SW-striking PGSZ that extends further west along the two dextrally offset branches of the North Ouessant Shear Zone (NOSZ) (Fig. 1b, c) (Le Gall et al., 2014). It is a composite intrusion, comprising three submassifs, namely the North Ouessant (NO), the West Aber-Ildut (W-AI) and the East Aber-Ildut (E-AI) submassifs. The complex cuts through metamorphic and granitic terranes of the Léon Domain (Figs. 1a and b) (Ballèvre et al., 2009; Faure et al., 2010).

The earlier and polyphased tectono-metamorphic history of the Léon hosted terranes started in the time-range 440-340 Ma with a HP metamorphic event, coeval to northerly-directed thrusting during an early oceanic subduction to collision phase. The following stage (340-300 Ma) resulted in the exhumation of deeply-buried units associated with migmatites in HT metamorphic conditions during a transtensional, and locally pure transcurrent shear regime, synchronously to multistage granitic intrusions (Paquette et al., 1987; Schultz et al., 2007; Marcoux et al., 2009; Faure et al., 2010; Schultz, 2013; Le Gall et al., 2014). Dextral shearing along the North Armorican Shear Zone (NASZ) was accompanied by the intrusion of the 316.0 ± 2.0 Ma (U /Pb zircon ages) St-Renan-Kersaint synkinematic granite (Le Gall et al., 2014). This event just predated the c. 300 Ma magmatic and tectonic activities studied in this paper, assigned to late syn-convergence processes in response to a NS-directed shortening.

3.2 Sampling and nomenclature

Most samples were collected in the northern part of the Ouessant Island (NO, Fig. 1c) and along the western coastal sector of the Aber-Ildut pluton (W-AI, Fig. 1d). Two additional samples were taken in the eastern sector of the Aber-Ildut pluton (E-AI, Fig. 1b) and one offshore sample (C34, Fig. 1b) was cored by gravity Cnexo-ville rock core (Le Gall et al., 2014). In addition to magmatic rocks, two metasedimentary xenoliths (AI11 and AI27) were sampled in the W-AI submassif (Fig. 1d).

Granitoid nomenclature is based on the Q' vs. ANOR diagram of Fig. 2, derived empirically by Streckeisen and Le Maitre (1979) from the IUGS classification of Streckeisen (1976) and considered as its CIPW normative equivalent. This diagram is based on the normative parameters 100Q/(Q + Ab + Or +An), representing silica saturation, and 100An/(An + Or) that reflects the relative abundance of calcium and potassium in the rocks. Sample OS11, which plots in the lower part of the Afs granite field, displays a mineralogy of Afs quartz microsyenite (see below) and, thus, will be considered as such. Lamprophyres are classified by using the $CaO\text{-}SiO_2/10\text{-}4TiO_2$ diagram of Rock (1987) in Fig. 3. AI lamprophyres plot in the calc-alkalic field.

3.3. Geochronology

The W-AI porphyritic monzogranite 13DB05 yielded a Concordia age of 303.8 ± 0.89 Ma (1 sigma, MSWD = 2.9), slightly older than its $^{206}Pb/^{238}U$ age of 302.8 ± 2.0 Ma (1 sigma, MSWD = 0.56) (Supplementary Table S1 and Fig. 4). This Concordia age is consistent with previously published ages of: 301.4 ± 4.3 Ma (U-Pb/TIMS) for the AI porphyritic monzogranite (Marcoux et al., 2009); 292.6 ± 2.7 Ma (Ar/Ar) for the PGSZ mylonites

(Marcoux et al., 2009). These ages typically concern one of the latest Variscan events in the Armorican Massif (see Ballèvre et al., 2009, for a review).

3.4 Field relationships

Granitoids located close to both the PGSZ and the NOSZ exhibit C/S-type tectonic fabrics indicating ductile sinistral shearing. Away from the shear zones, granitoids are nearly unstrained and still contain preserved magmatic flow structures outlined by Afs megacryst orientation and elongated enclaves (Fig. 5a).

Porphyritic monzogranites (Fig. 5a, b, d) form the main part of the Aber-Ildut pluton, since constituting two-thirds of the W-AI submassif (Fig. 1d), and cropping out locally in the eastern sector (Fig. 1b). Porphyritic syenogranites occur in the southern sector of the W-AI submassif, but not at its edge (Fig. 1d), and in the central part of the Ouessant Island (Fig. 1c). Two-mica leucogranites are the prominent facies in the E-AI submassif (Fig. 1b). They also occur as intrusive bodies of various sizes in the W-AI submassif (Fig. 1d). Mingling structures, observed north of the W-AI submassif, reveal that the monzogranites have been intruded by the leucogranites prior to their complete solidification. The northern part of Ouessant is exclusively composed of two-mica leucogranites (Figs. 1c and 5c, e). Sample C34 confirms the extension of this facies offshore (Fig. 1b). Microgranites constitute a dense NS-trending dyke network cutting through the central part of the W-AI submassif (Fig. 1d). They are a few meters wide and can be up to 3 km long. The systematic presence of fine-grained chilled margins typically attests that their emplacement postdates the crystallization of their granitic host. Tourmaline-bearing leucogranites are exposed at the southern edge of the W-AI submassif (Fig. 1d).

Very abundant ovoid quartz-monzodioritic or granodioritic enclaves are included in monzo-/syenogranites in the W-AI submassif (Fig. 1d). In some cases, it can be noticed that orthose megacrysts have migrated from the host granite into enclaves, hence demonstrating that both granodiorites and quartz monzodiorites were liquid at the time of their incorporation into granites (Fig. 5a). Along the NS coastal section, the orientation of elongated enclaves changes southwards from a N70°E direction, i.e. parallel to the PGSZ, to a submeridian orientation, i.e. nearly perpendicular to the PGSZ (Fig. 1d). Two large areas of quartz monzodiorites, with mingling structures (Fig. 5c), are exposed in the Ouessant Island (Fig. 1c).

Two kinds of ultrapotassic dykes are identified in the AI-NO complex: calc-alkalic lamprophyres in the W-AI submassif and alkali feldspar (Afs) quartz microsyenites in North-Ouessant. Lamprophyric dykes are a few meters wide and can be up to several hundred meters long (Fig. 5d). They have a NS direction, consistent with a submeridian compression (Rolet et al., 1986). Their emplacement predates the end of crystallization of their monzo-/syenogranitic host-rocks, as evidenced by the presence of mingling structures along the contact. By contrast, in the North Ouessant area, unstrained dykes of Afs quartz microsyenites postdate their sheared two-mica leucogranite host-rock.

4. Petrology and mineralogy

4.1. Porphyritic monzogranites

Porphyritic monzogranites are typically characterized by 35 x 15 mm-sized (sometimes > 50 mm) red orthoclase megacrysts (Fig. 5b). Their color is probably due to iron oxide impurities (Chauris, 1994). Quartz, andesine, apatite-bearing biotite, ilmenite and rare

titanite and zircon are also present. Muscovite and amphibole are lacking. Monzogranite biotites plot at the boundary between calc-alkalic and peraluminous fields in the discrimination diagram of Abdel-Rahman (1994) in Fig. 6a.

4.2. Syenogranites

To the naked eyes, porphyritic syenogranites resemble the previous monzogranite facies. However, the orthoclase megacrysts are slightly smaller and generally colorless, except in Ouessant, where they are red. The mineralogy of porphyritic syenogranites differs from those of monzogranites with the oligoclase composition of its plagioclases, as well as with the presence of very few muscovite crystals. The gradual transition from the porphyritic monzogranitic facies into the syenogranitic one is part of the spatial magmatic zonation leading progressively to the W-AI south border facies (Fig. 1d).

The two-mica syenogranites form a first peripheral strip in the southern part of the W-AI submassif: they crop out south of the porphyritic syenogranites and in the southeastern edge of the area (Fig. 1d). The corresponding rocks have a coarse texture and contain only sparse orthoclase megacrysts. The muscovite/biotite ratio increases progressively southwards: biotite is more abundant than muscovite in the northern part of the strip and the opposite is true near the limit with the southern leucogranites (Chauris, 1994).

All syenogranite biotites plot in the peraluminous field in the Fig. 6a discrimination diagram.

4.3. Alkali feldspar leucogranites

The two-mica (micro)leucogranites display varied petrographic facies (presence or not of a few alkali feldspar megacrysts, coarse- versus fine-grained size, variable muscovite/biotite ratio), but all of them are clear-colored and contain orthoclase or microcline, quartz, oligoclase-albite, muscovite, biotite, apatite, and sometimes zircon. Andalusite crystals have been identified in the sample AI19 (Supplementary Table S2). Late- to post-magmatic tourmaline occurs as either disseminated cluster or tourmaline-filled veins.

Tourmaline leucogranites are very clear rocks containing dark tourmaline crystals, often more than 1 cm long, disseminated in the groundmass. Note that the AI3a tourmalines are more magnesian that the AI2 ones (Supplementary Table S2). The only other colored mineral is poikilitic red garnet, a few millimeters in diameter (Fig. 5f). Its composition is dominated by almandine (0.71 - 0.61) and spessartine (0.28 - 0.38) (Supplementary Table S2). Biotite is lacking. Colorless minerals are microcline, albite, quartz and muscovite (Fig. 5f). Near the AI2 sampling point (Fig. 1d), a greisen-type alteration results locally in newly-formed quartz and muscovite (Chauris, 1994). Tourmaline and garnet are resistant to this alteration.

All leucogranite biotites plot in the peraluminous field in Fig. 6a.

4.4. Enclaves

4.4.1. Granodiorites and quartz monzodiorites

The corresponding dark and fine-grained rocks contain plagioclase, quartz, orthose, biotite, titanite, Fe-Ti oxides and minor apatite; green hornblende occurs in the quartz monzodiorite OS1. Quartz monzodiorites only differ from granodiorites by their greater plagioclase content, present as phenocrysts in the sample AI28. Biotites in the granodiorite AI6b plot in the peraluminous field in Fig. 6a, near the boundary with the calc-alkalic field.

294

295 *4.4.2. Metasedimentary xenoliths*

296 Sample AI11 is a diatexite made up of large leucocratic veins (quartz, orthose,
297 plagioclase, muscovite, biotite and minor apatite), together with a diffuse restite network of
298 biotite-rich veinlets. Sample AI27 is an ancient pelitic rock recrystallized into hornfels. It is
299 composed of a fine-grained matrix of polygonal quartz, biotite and plagioclase, crossed by
300 thin coarse-grained leucocratic veins, containing perthitic orthoclase, quartz and subordinate
301 biotite. Muscovite is confined to some narrow zones, which might outline previous
302 sedimentary beds with different composition.

303

304 *4.5. Ultrapotassic dykes*

305

306 Lamprophyres are melanocratic hypabyssal igneous rocks with porphyritic fine-
307 grained textures carrying hydrous mafic phenocrysts (Rock, 1987, 1991). Feldspars are
308 generally restricted to the groundmass (Prelević et al, 2004). Calc-alkalic lamprophyres are
309 commonly associated with granites of same affinity. Aber-Ildut lamprophyres are mica-phyric
310 fine-grained rocks (Fig. 5g). The brown mica phenocrysts, up to 2 mm long, have a Mg-Ti-
311 rich biotite composition. They can form clusters, a few millimeters in diameter. Groundmass
312 micas are also biotites, or Fe-rich phlogopites, which have a less pronounced brown color.
313 Biotites plot in the calc-alkalic field in Fig. 6a; biotites and phlogopites plot in the calc-alkalic
314 lamprophyre fields in the discrimination diagrams of Rock (1987) in Fig. 6b. The other
315 primary phases are: orthoclase, which forms the main part of the groundmass, quartz,
316 sometimes corroded, rare plagioclase, augite-diopside, and apatite, quite abundant in the
317 groundmass, which also occurs in the form of 2 mm-long phenocrysts in a few samples.
318 Alteration is expressed by kaolinization of K-feldspars, partial chloritization of micas and

amygdale filling with quartz and epidote. These calc-alkalic lamprophyres have a minette-type mineralogy (biotite phenocrysts and alkali feldspar dominant in the groundmass), according to the criteria of Rock (1991) and Prelević et al. (2004).

Although the dyke sample OS11 plots in the alkali feldspar granite field (Fig. 2), its mineralogy is rather consistent with that of an alkali feldspar quartz microsyenite. It is a subaphyric cryptocrystalline rock. Small phenocrysts of orthose, chloritized biotite, sparse altered oligoclase and euhedral apatite are immersed in a groundmass mainly made up of orthose, quartz, and subordinate biotite and augite. Secondary quartz, sometimes surrounded by chlorite needles, fills a few spherical amygdales.

5. Geochemistry

5.1. Major elements

All the AI-NO available major and trace element compositions are presented in Table 1. Among the four geochemical discrimination diagrams versus SiO_2 shown in Fig. 7, three of them were used by Frost et al. (2001) in their classification scheme, whereas the fourth one is the classical K_2O-SiO_2 diagram of Peccerillo and Taylor (1976).

The Fe* diagram in Fig. 7a can be used to distinguish ‘magnesian’ from ‘ferroan’ granitoids, as proposed by Frost et al. (2001). Samples that plot in the magnesian field have not necessarily mole proportion of Mg higher than Fe, they are just relatively Mg enriched compared with the whole population of granitoids. Following Frost et al. (2001), magnesian compositions would be consistent with hydrous, oxidizing magmas. All the AI-NO analyzed samples are magnesian, except one syenogranite and the more silicic leucogranites.

The MALI (modified alkali-lime index) diagram in Fig. 7b allows the characterization of granitoid compositional series. With the exception of the ultrapotassic rocks and one tourmaline leucogranite, all the AI-NO analyzed magmatic samples follow – or are very close to – the alkali-calcic trend. This feature, also visible in the Q'-ANOR diagram in Fig. 2, has been considered elsewhere as a specific attribute of post-tectonic Paleozoic granitoids in the Irish and British Variscides (Frost et al., 2001).

The ASI (aluminium saturation index) diagram in Fig. 7c can be used to discriminate peraluminous (ASI > 1) from metaluminous (ASI < 1; Na + K < Al) and peralkaline rocks (ASI < 1; Na + K > Al). The expression of the ASI, including P_2O_5 (Fig. 7c), takes into account the presence of apatite. If ASI > 1.1, rocks are considered as strongly peraluminous (SP) (Sylvester, 1998). The SP granites are commonly thought to originate from a pure sedimentary source (Sylvester, 1998; Frost et al., 2001). The whole set of the AI-NO analyzed samples – except one lamprophyre and the NO quartz monzodiorite – is peraluminous; all the leucogranites are strongly peraluminous, together with most of the syenogranites. Peraluminosity increases roughly with SiO_2.

The K_2O versus SiO_2 diagram in Fig. 7d shows that the AI-NO plutonic association corresponds to a high-K/ultra-K magmatism. The Afs quartz microsyenite OS11 plots high above the high-K/shoshonitic limit, together with the hornfelds AI27. Lamprophyres have also very high K_2O contents (> 5 wt %) and plot in the calc-alkalic lamprophyre field of Rock (1987).

The SiO_2 and MgO contents of the AI-NO calc-alkalic lamprophyres (55.5 – 57.3 and 3.6 – 3.8 wt%, respectively, Table 1) matches those of western Serbia leucominettes (50.5 < SiO_2 < 61.0 wt%; 2.6 < MgO < 7.5 wt%: Prelević et al., 2004). They are distinct from the post-Variscan Mg-rich minettes of SW England (48.0 < SiO_2 < 52.9 wt%; 5.3 < MgO < 8.1

wt%: Leat et al., 1987; see also Figs. 3 and 7d), despite similar geological context and age (c. 290 Ma).

Variations of MgO, Al_2O_3, and P_2O_5 relative to SiO_2 are rather regular from leucominettes to leucogranites (Fig. 8a-c). It can be noticed that (1) the quartz monzodiorite AI28 and the hornfels AI27 are enriched in Al_2O_3 (> 17 wt%) with respect to the other samples; (2) the ultrapotassic rocks are especially enriched in P_2O_5, which reflects the abundance in apatite; and (3) the Afs quartz microsyenite OS11 has a composition that plots between the leucominettes and the porphyritic syenogranites.

5.2. Trace elements

A selection of trace elements having contrasted magmatic behaviors is shown in function of SiO_2 in the diagrams in Fig. 8d-f. Except for the ultrapotassic rocks and the metasedimentary xenoliths, the evolutionary trends of Ba, Eu and Y are fairly regular. Leucominettes are characterized by high Y and Eu values, and more especially by huge Ba contents (> 5000 ppm). The Afs quartz microsyenite displays geochemical features comparable, but attenuated, to those of the lamprophyres.

AI-NO moderately peraluminous (MP) rocks (quartz monzodiorites, granodiorites and monzogranites) are enriched in light and middle rare earth elements (LREE and MREE, respectively) with respect to heavy REE (HREE). The corresponding distribution patterns are very close to each other (Fig. 9a).

AI-NO strongly peraluminous (SP) granitoids (syenogranites – Fig. 9a – and leucogranites – Fig. 9b) display lower REE patterns, with more marked Eu anomalies. Note the remarkable resemblance between the patterns of OS4 (NO two-mica leucogranite) and AI32 (W-AI two-mica microleucogranite), in agreement with the other geochemical diagrams

(Figs. 2, 7, 8). Compared with the two-mica rocks, the tourmaline leucogranites AI2 and AI3a are depleted in REE (except in Yb and Lu) and especially in Eu. In addition, their REE behavior does not gradually change into smooth curvilinear patterns, as usual, from La to Lu: the lanthanides can be subdivided into four groups with different pattern shapes, separated by slope breaks (Fig. 9b). In particular, groups 1 (La, Ce, Pr, Nd) and 3 (Gd, Tb, Dy, Ho) are characterized by the parallelism of the corresponding AI2 and AI3a concave-down curve sectors.

5.3. Isotopes

The Sr and Nd isotopic ratios are presented in Table 2. In the ε^{t}_{Nd} vs. initial $^{87}Sr/^{86}Sr$ (t = 304 Ma) diagram in Fig. 10a, there are clear relationships between the isotopic composition and the petrologic characteristics of the samples. The MP granitoid samples (AI6b and AI26) plot close to both the leucominette AI33 and the Afs quartz microsyenite OS11 ($0.705613 < {}^{87}Sr/^{86}Sr_i < 0.706609$; $-3.00 < \varepsilon^{304}_{Nd} < -1.58$; Table 2); the SP leucogranitic samples have higher initial $^{87}Sr/^{86}Sr$ ratio and lower initial ε_{Nd} ($0.706538 < {}^{87}Sr/^{86}Sr_i < 0.713548$; $-5.43 < \varepsilon^{304}_{Nd} < -4.36$). The migmatite AI11 has a leucogranite-type isotopic composition ($^{87}Sr/^{86}Sr_i = 0.709571$; $\varepsilon^{304}_{Nd} = -5.29$); by contrast, the hornfels AI27 displays an original isotopic composition, with a high $^{87}Sr/^{86}Sr$ ratio (0.719068) and a very low ε^{304}_{Nd} of -12.17 (Table 2). The isotopic compositions of the AI-NO hornfels and leucogranites fit with those of pelites and peraluminous late-Variscan granites, respectively, from the Spanish Central Region (Fig. 10a) (Villaseca et al., 1998).

6. Discussion

6.1. Emplacement of the AI-NO complex

The preferred orientation of quartz monzodiorite/granodiorite enclaves in the coastal W-AI submassif (i.e., parallel to the PGSZ near the shear zone, perpendicular to the PGSZ southwards, and randomly oriented close to the southern edge, Fig. 1d), once combined to the petrological data presented in section 4, is consistent with the following two-stage emplacement model previously applied by Jamgotchian (1986) and Chauris (1991, 1994) to the AI pluton.

A first magmatic arrival rose through the PGSZ conduit, before injecting southward as a huge horizontal sill (Fig. 11). The observed north-south compositional gradient implies that tourmaline leucogranites were emplaced prior to syenogranites that in turn predate monzogranites. As a first approximation, the progressive petrological transition, marked by a noticeable muscovite enrichment southwards, could be consistent with the existence of a stratified reservoir at depth, with leucocratic magmas at the top and monzogranitic (± Q-monzo/granodioritic) liquids at the bottom. Another possibility would be to consider disconnected evolution of heterogeneous liquids within different reservoirs, with magmas using a same pathway when emplaced in the upper crust. A similar crustal ascent path through the NOSZ can be envisaged for the Ouessant porphyritic syenogranite.

During the second stage, two-mica leucogranitic bodies were intruded along the PGSZ/NOSZ, before the end of crystallization of the first injection. They currently form the northern part of the W-AI pluton, nearly all the E-AI pluton, and the northern sector of Ouessant. Field relationships suggest that the other occurrences of two-mica leucogranites, such as C34- and AI5-type intrusions (Fig. 1b, d), could correspond to residual inliers of eroded initially horizontal sill units, overlying syeno-/monzogranites that rooted further north along the PGSZ/NOSZ (Fig. 11).

Finally, the AI-NO complex was intruded by three distinct dyke swarms comprising: (1) leucominettes, emplaced before the end of crystallization of the previous units; (2) two-mica microleucogranites, and (3) Afs quartz microsyenites, both postdating crystallization in the plutonic complex.

6.2. Petrogenesis of the SP/MP granitoids

The proposed emplacement model for the AI-NO complex is consistent with one or several reservoir(s) containing both strongly (SP) and moderately peraluminous (MP) magmas, but it leads to questions about the source of these two types of magmas and the possible genetic links between them.

Although fractional crystallization is a process invoked by several authors to explain chemical variations in various granitic complexes (e.g., Cocherie et al., 1994; Ramírez and Grundvig, 2000), such a mechanism is unsuitable in the AI-NO case, for two reasons: (1) pure fractional crystallization is not consistent with variations of initial isotopic ratios (Fig. 10a), and (2) subaluminous minerals (e.g., amphibole, apatite, titanite), likely to increase peraluminosity in silicic residual liquids by fractionating, are either absent or rare in the studied rocks.

Assimilation coupled with fractional crystallization (AFC) might be a key to resolve these two problems. Indeed, crustal contamination might have caused both isotopic variations and increase in the peraluminosity degree from MP to SP magmas. Results of Villaseca et al. (1998) about Variscan granitic batholiths of Spanish Central Region (CSR), displaying Sr-Nd isotopic compositions of both granitic and country rocks comparable to those of the AI-NO complex (Fig. 10a), have shown that: (1) AFC modeling implies either an unrealistically high mantle contribution (for a pelitic contamination) or an excessively elevated assimilation rate

(for a contamination with meta-igneous material), and (2) none of the metamorphic country rocks has the appropriate isotopic composition to satisfy the origin of the granites. It has been noted above about the AI metasedimentary samples that only the initial Sr-Nd isotopic composition of the migmatite AI11 matches those of the strongly peraluminous AI-NO granites (Fig. 10a). The hornfels AI 27 have a less radiogenic $^{143}Nd/^{144}Nd$ initial ratio and a more radiogenic $^{87}Sr/^{86}Sr$ initial ratio than the granites (Fig. 10a). Consequently, it cannot be regarded as a potential contaminant in an AFC model. Such a feature corresponds to that described by Villaseca et al. (1998).

Most authors consider that SP granites strictly originate from crustal melting processes (Sylvester, 1998; Ramírez and Grundvig, 2000; Frost et al., 2001; Eyal et al., 2004; Antunes et al., 2008), whereas MP high-K calc-alkalic/alkali-calcic granites instead would result from interaction between crustal- and mantle-derived melts (Wenzel et al., 1997; Rottura et al., 1998; Sylvester, 1998; Patiño Douce, 1999; Eyal et al., 2004) (see section 6.5. for a detailed discussion of this second point about AI-NO granitoids). In this way, Villaseca et al. (1998) have proposed a crustal-derived model, with limited-scale mixing between mafic and felsic magmas, to account for the genesis of the Central Spain SP/MP peraluminous granites. To explain the isotopic difference between metapelites and granites, they considered the possibility of disequilibrium partial melting in high-grade anatectic areas. Indeed, Barbero et al. (1995) showed that the pelite-derived anatectic leucogranites from Toledo (Spain) have systematically higher initial ε_{Nd} and lower initial $^{87}Sr/^{86}Sr$ than the regional unmelted metapelites. Such initial isotopic differences between a protolith and its melted products are thought to be controlled by both the kinetic of the melting and the stoichiometry of the reaction (Hammouda et al., 1994). Following Barbero et al. (1995) and Villaseca et al. (1998), the differences would result from an enrichment in biotite and accessory minerals of the migmatitic mesosomes, relative to the leucosomes during partial melting (Fig. 10b). In the AI-

492 NO complex under study, the isotopic difference observed between the slightly melted
493 metapelitic hornfels AI27 and the leucosome-rich migmatite AI11 could be satisfactorily
494 explained by such an isotopic disequilibrium model (arrow in Fig. 10a). Consequently, in
495 spite of their contrasted initial isotopic composition, the couple AI11/AI27 could be a good
496 candidate for matching the – probably heterogeneous – protolith of the AI-NO strongly
497 peraluminous leucogranites.
498
499 *6.3. Tetrad effect in leucogranites*
500
501 The tetrad effect, first defined by Peppard et al. (1969), reflects a process affecting the
502 REE complexing behavior (Bau, 1997; Irber, 1999). Masuda et al. (1987) described concave-
503 down tetrad REE patterns in extracted magmatic liquids. Since then, such specific REE
504 patterns have been observed in several highly silicic granites (Bau, 1997; Irber, 1999; Jahn et
505 al., 2001). In chondrite-normalized REE diagrams, the tetrad effect is readily identifiable by
506 the presence of four sectors of four elements separated at three positions: between Nd and Pm;
507 at Gd; and between Ho and Er. The tetrad effect is generally accompanied by modified
508 geochemical behavior of many non-REE trace elements, leading to variations in ratios known
509 to remain constant, such as K/Rb, K/Ba or Zr/Hf (Irber, 1999; Jahn et al., 2001).
510 REE patterns of the two W-AI tourmaline leucogranites seem to reveal a tetrad effect,
511 with the individualization of four sectors, numbered from 1 to 4 in Fig. 9b. To test this
512 hypothesis, and also to find out if that process affects other AI-NO granites, we have plotted
513 in Fig. 12 two diagrams with trace element ratios known to be sensitive to tetrad effect (K/Ba
514 and Eu/Eu*) in function of the parameter $TE_{1,3}$ of Irber (1999). The latter expression,
515 developed in Table 1, can be used to quantify the degree of tetrad effect on the first and third
516 REE tetrads, where the phenomenon is generally most obvious. K/Ba is positively correlated

517 with $TE_{1,3}$ (Fig. 12a), whereas Eu/Eu* is negatively correlated (Fig. 12b). The latter diagram
518 shows clear correlation between magnitude of the Eu anomaly and the degree of tetrad effect.
519 It follows that the tetrad effect concerns, to a varying degree, all the AI-NO granites, all the
520 more so as they are silicic.

521 The tetrad effect reflects the influence of chemical complexation. It is commonly
522 interpreted as the result of the opening of a magmatic system at the ultimate stages of its
523 evolution, with intense interaction of the residual melts with F- and Cl-rich aqueous
524 hydrothermal fluids (Irber, 1999; Jahn et al., 2001). In the AI pluton, it might be in relation
525 with the greisen alteration observed close to the AI2 sampling point.

526

527 *6.4. Origin of the ultrapotassic rocks*

528

529 The origin of the calc-alkalic lamprophyres is still a matter of debate. However, there
530 is consensus to consider minettes as representing small-degree melts that form within the
531 lithospheric mantle at depths ≥ 50 km (Rogers et al., 1982; Wyman and Kerrich, 1993). Their
532 unusual geochemistry is generally explained by partial melting of a lithospheric mantle source
533 metasomatized by fluids derived from subducted material (Carmichael et al., 1996; Wenzel et
534 al., 1997; Hoch et al., 2001). More felsic minettes or leucominettes have been interpreted by
535 Prelević et al. (2004) as the result of hybridization between crustal-derived dacite-type
536 magmas and mantle-derived lamproitic melts, an idea previously put forward by Rock (1991).
537 Following Prelević et al. (2004), such a mixing mechanism is thought to be universally
538 applicable to the origin of (leuco)minettes associated with granites in late- or post-orogenic
539 settings.

540 The isotopic composition of the leucominette AI33, close to that of the granodiorites
541 and the monzogranites (Fig. 10a), is neither purely mantellic (i.e. with positive ε^{t}_{Nd}) nor

purely crustal (i.e. close to the SP granite composition). This feature suggests that leucominettes likely result from mixing – or interaction – between crustal- and mantle-derived products, in agreement with the model of Prelević et al. (2004).

In many diagrams in Fig. 8, the Afs quartz microsyenite OS11 plots in lines linking leucominettes and porphyritic syenogranites. To check the hypothesis that OS11 resulted from a mixing between these two magmatic types, a mass balance calculation test on major elements (least-square approach of Wright and Doherty, 1970) has been performed with the porphyritic syenogranite AI7 and the leucominette 13DB07. This test indicates that OS11 possibly originates by mixing 46.6 % of AI7 with 53.4 % of 13BD07 (sum of the squared residuals $\Sigma R^2 = 1.03$, with weighting factors of 0.5 for CaO and K_2O). Such a model is consistent with the isotopic similarity between the leucominette AI33, the monzogranite AI26 – the syenogranite AI7, not analyzed for isotopes, is thought to have a similar isotopic composition – and OS11 (Fig. 10a). Nevertheless, additional fractionation/accumulation of MREE-bearing minerals (such as apatite) is required to account for the respective shapes of AI7 and OS11 REE patterns (Fig. 9b).

6.5. Multistage mixing

It has been argued in section 6.4. that the AI leucominettes might result from hybridization between crustal- and mantle-derived materials, probably between SP-type and lamproitic melts (Prelević et al., 2004). In addition, the NO Afs quartz microsyenite OS11 is interpreted as the mixing product of syenogranitic and lamprophyric magmas. Finally, many authors suggested that MP calc-alkalic/alkali-calcic granites also result from interaction between crustal- and mantle-derived melts (Patiño Douce, 1999; Eyal et al., 2004).

In order to address these several mixing hypotheses, the AI-NO data are plotted in Patiño Douce's (1999) diagrams, together with field contours of various peraluminous granites and experimental curves (Fig. 13), and in Sylvester's (1998) diagrams, especially devoted to SP granites (Fig. 14), where calculated curves are also indicated.

In Fig. 13 diagrams, the AI-NO SP granites plot into the leucocratic field of Patiño Douce (1999), whereas the AI-NO MP granitoids fit with S-type granites. In the three diagrams in Fig. 13, mafic pelites are located near the intersection of leucocratic and S-type fields (Patiño Douce, 1999). The reaction curves model the melt compositions produced by hybridization of olivine tholeiite with metapelite both at high (1.2-1.5 GPa) and low pressures (< 0.5 GPa). These diagrams imply that: (i) the AI-NO SP leucogranites have a crustal origin, perhaps pelitic; (ii) if the metasedimentary xenoliths AI11 and AI27 represent really the protolith, as suggested by their isotopic compositions in Fig. 10a, their major element chemistry has apparently been slightly modified during melting and metamorphism; (iii) the AI-NO MP granitoids – plus leucominettes and OS11 – can result from mixing between pelitic-derived melt(s) and mafic liquid(s); (iv) mixing occurs at low pressures ($\leq$ 0.5 GPa) (Fig. 13b, c).

The CaO/Na_2O vs. Al_2O_3/TiO_2 diagram in Fig. 14a shows the late-orogenic SP granites field defined by Sylvester (1998), together with a mixing curve between basalt and pelite-derived melt (see Fig. 14a for more details). All the AI-NO syeno- and leucogranites plot within the Sylvester's (1998) SP field, except the tourmaline-leucogranites. The AI-NO MP granitoid field, to which can be added leucominettes and OS11, extends parallel to the mixing curve, slightly shifted to the left. This feature can be interpreted as indicating that the AI-NO MP granitoids result from mixing between both pelite-derived melts and mafic magmas slightly different from those used for the modeling. By contrast, the AI-NO MP data fit perfectly with the calculated mixing curve between similar components in the Rb/Ba vs.

Rb/Sr diagram in Fig. 14b. Note that leucominettes plot just near the basalt end-member. The most probable source for the AI-NO SP granites is clay-rich pelitic materials. Tourmaline-leucogranites display very high Rb/Sr and Rb/Ba ratios, probably in response to the tetrad effect, which affects them (Fig. 12). The migmatite AI11 plots very close to the calculated pelite-derived melt.

Analyzing the diagrams in Figs. 13 and 14 confirms that the geochemical diversity of the AI-NO granitoid complex likely results from mixing of different end-members material comprising (1) a clay-rich pelitic (crustal) component, (2) mantle-derived lamproitic, and/or (3) mafic melts. In any case, mantle metasomatism is a plausible mechanism to explain the genesis of fluid-rich lamprophyric products – i.e. unsampled lamproites and/or mafic minettes, thought to be at the origin of the analyzed leucominettes by hybridization with crustal liquids. Late-orogenic AI-NO granitoids probably formed at low pressure (Figs. 13b and c), in agreement with metamorphic and structural data indicating that, at 330-290 Ma, the Leon Domain is the locus of strong crustal exhumation and transtension (Schulz et al., 2007; Le Gall et al., 2014). These granitoids are thus produced by lithospheric thinning with advective heating of a $\leq$ 50 km-thick crust from hot metasomatized asthenosphere (Sylvester, 1998) (Fig. 15). As underlined by Patiño Douce (1999), the nature of the chemical interactions between the continental crust and invading mafic magmas is probably complex, and assimilation, fractional crystallization, crystal accumulation and fluid transfer processes might have interfered in addition to multistage magma mixing.

7. Conclusions

1. The late-Variscan Aber-Ildut/North-Ouessant (AI-NO) complex is an association of late-orogenic high-K alkali-calcic granitoids dated at 303.8 ± 0.89 Ma. It comprises an early

magmatic intrusion that rooted vertically along the PGSZ/NOSZ conduit, before being injected southwards as a huge horizontal zoned sill. A progressive enrichment in muscovite southwards can be noted. A second magmatic stage resulted in the intrusion of a large leucogranitic body, prior to the end of crystallization of the first injection. During a last stage, the complex is intruded by three dyke swarms of leucominette, microleucogranite and quartz microsyenite.

2. The main petrogenetic processes at the origin of the various petrographic types sampled in the AI-NO complex are melting of crustal clay-rich pelitic material and mixing of the resulting magmas with mantle-derived products. The strongly peraluminous (SP) granites are interpreted as pure melting products. All the other petrographic types (moderately peraluminous granitoids, leucominettes and quartz microsyenites) are thought to result from mixing between crustal melts and mantle-derived mafic liquids. The more silicic granites were affected by a tetrad effect, in relation with REE complexing behavior.

3. AI-NO granitoids probably formed at low pressure, during the Variscan late-orogenic stage associated with exhumation, transtension, HT metamorphism and lithospheric thinning, by advective heating of a $\leq$ 50 km-thick crust from hot metasomatized asthenosphere.

Supplementary data to this article can be found online at…

Acknowledgements

Field studies were conducted in 2013 and 2014. Detailed and constructive comments by two anonymous reviewers helped us to improve the text. The authors are grateful to J. Langlade (microprobe analyses), C. Bollinger (ICP-MS Brest), P. Nonnotte (TI-MS), C. Liorzou (ICP-AES), M.-L. Rouget (chemistry lab assistant, UMS n°3113), A. von Quadt

(U/Pb geochronology, ETH Zurich), P. Vonlanthen (Scanning electron microscopy, Institut des Sciences de la Terre, Lausanne), P. Tieffenbach (thin sections), and J.-P. Oldra (sample preparation). DBG has benefited from a Swiss National Science Foundation (SNSF) grant no. PA00P2-145309. Many thanks to J.-A. Barrat for having detected the tetrad effect.

References

Abdel-Rahman, A.M., 1994. Nature of biotites from alkaline, calc-alkalic, and peraluminous magmas. Journal of Petrology 35, 525-541.

Antunes, I.M.H.R., Neiva, A.M.R., Silva, M.M.V.G., Corfu, F., 2008. Geochemistry of S-type granitic rocks from the reversely zoned Castelo Branco pluton (central Portugal). Lithos 103, 445-465.

Ballèvre, M., Bosse, V., Ducassou, C., Pitra, P., 2009. Paleozoic history of the Armorican Massif. Models for the tectonic evolution of the suture zones. Comptes Rendus Geoscience 341, 174-201.

Barbarin, B., 1999. A review of the relationships between granitoid types, their origins and their geodynamic environments. Lithos 46, 605-626.

Barbero, L., Villaseca, C., Rogers, G., Brown, P.E., 1995. Geochemical and isotopic disequilibrium in crustal melting: An insight from the anatectic granitoids from Toledo, Spain. Journal of Geophysical Research 100, 15 745-15 765.

Barrat, J.A., Blichert-Toft, J., Gillet, Ph., Keller, F., 2000. The differentiation of eucrites: The role of *in situ* crystallization. Meteoritics and Planetary Science 35, 1087-1100.

Barrat, J.A., Keller, F., Amossé, J., Taylor, R.N., Nesbitt, R.W., Hirata, T., 1996. Determination of rare earth elements in sixteen silicate reference samples by ICP-MS after Tm addition and ion exchange separation. Geostandards Newsletter 20, 133-139.

666 Barrat, J.A., Zanda, B., Moynier, F., Bollinger, C., Liorzou, C., Bayon, G., 2012.
667 Geochemistry of CI chondrites: Major and trace elements, and Cu and Zn isotopes.
668 Geochimica et Cosmochimica Acta 83, 79-92.
669 Bau, M., 1997. The lanthanide tetrad effect in highly evolved felsic igneous rocks – A reply to
670 the comment by Y. Pan. Contributions to Mineralogy and Petrology 128, 409-412.
671 Berthé, D., Choukroune, P. Jegouzo, P., 1979. Orthogneiss, mylonite and non coaxial
672 deormation of granites : the example of the South Armorican Shear Zone. Journal of
673 Structural Geology 1, 31-42.
674 Carmichael, I.S.E., Lange, R.A., Luhr, J.F., 1996. Quaternary minettes and associated
675 volcanic rocks of Mascota, western Mexico: a consequence of plate extension above a
676 subduction modified mantle wedge. Contributions to Mineralogy and Petrology 124,
677 302-333.
678 Chappell, B.W., White, A.J.R., 1974. Two contrasting granite types. Pacific Geology 8, 173-
679 174.
680 Chauris, L., 1991. Le granite à tourmaline de Plouarzel (Finistère) : aspects chimico-
681 minéralogiques d'une différenciation marginale leucogranitique. Géologie de la France
682 4, 31-38 (in French).
683 Chauris, L., 1994. Notice explicative, Carte géologique de la France (1/50 000), feuille
684 Plouarzel–île d'Ouessant (237). Orléans, BRGM Éditions, 132 p. (in French).
685 Chauris, L., Hallégouët, B., 1989. Notice explicative, Carte géologique de la France (1/50
686 000), feuille Le Conquet (273). Orléans, BRGM Éditions, 69 p. (in French).
687 Cocherie, A., Rossi, P., Fouillac, A.M., Vidal, P., 1994. Crust and mantle contribution to
688 granite genesis. An example from the Variscan batholith of Corsica, France, studied by
689 trace-element and Nd–Sr–O-isotope systematics. Chemical Geology 115, 173-211.

690 Condie, K.C., 1993. Chemical composition and evolution of the upper continental crust:
691 contrasting results from surface samples and shales. Chemical Geology 104, 1-37.
692 Cotten, J., Le Dez, A., Bau, M., Caroff, M., Maury, R., Dulski, P., Fourcade, S., Bohn, M.,
693 Brousse, R., 1995. Origin of rare-earth element and yttrium enrichments in subaerial
694 exposed basalts: evidence from French Polynesia. Chemical Geology 119, 115-138.
695 Downes, H., Duthou, J.L., 1988. Isotopic and trace element arguments for the lower-crustal
696 origin of Hercynian granitoids and pre-Hercynian orthogneisses, Massif Central
697 (France). Chemical Geology 68, 291-308.
698 Eyal, M., Litvinovsky, B.A., Katzir, Y., Zanvilevich, A.N., 2004. The Pan-African high-K
699 calc-alkalic peraluminous Elat granite from southern Israel: geology, geochemistry and
700 petrogenesis. Journal of African Earth Sciences 40, 115-136.
701 Faure, M., Sommers, C., Melleton, J., Cocherie, A., Lautout, O., 2010. The Léon domain
702 (French Massif armoricain): a westward extension of the Mid-German Crystalline Rise?
703 Structural and geochronological insights. International Journal of Earth Sciences 99, 65-
704 81.
705 Frost, B.R., Barnes, C.G., Collins, W.J., Arculus, R.J., Ellis, D.J., Frost, C.D., 2001. A
706 geochemical classification for granitic rocks. Journal of Petrology 42, 2033-2048.
707 Hammouda, T, Pichavant, M., Chaussidon, M., 1994. Mechanism of isotopic equilibration
708 during partial melting : an experimental test of the behaviour of Sr. Mineralogical
709 Magazine A 58, 368-369.
710 Hoch M., Rehkämper, M., Tobschall, H.J., 2001. Sr, Nd, Pb and O isotopes of minettes from
711 Schirmacher Oasis, East Antarctica: a case of mantle metasomatism involving
712 subducted continental material. Journal of Petrology 42, 1387-1400.

713 Irber, W., 1999. The lanthanide tetrad effect and its correlation with K/Rb, Eu/Eu*, Sr/Eu,
714 Y/Ho, and Zr/Hf of evolving peraluminous granite suites. Geochimica et Cosmochimica
715 Acta 63, 489-508.
716 Jahn, B.M., Wu, F., Capdevila, R., Martineau, F., Zhao, Z., Wang, Y., 2001. Highly evolved
717 juvenile granites with tetrad REE patterns: the Woduhe and Baerzhe granites from the
718 Great Xing'an Mountains in NE China. Lithos 59, 171-198.
719 Jamgotchian, A., 1986. Interférences d'effets cisaillants tangentiel et transcurrent: la mise en
720 place syntectonique du pluton granitique de l'Aber-Ildut (Nord-Finistère). Rennes,
721 Université de Rennes 1, Mémoire de DEA, 75 p. (in French).
722 Leat, P.T., Thompson, R.N., Morrison, M.A., Hendry, G.L., Trayhorn, S.C., 1987.
723 Geodynamic significance of post-Variscan intrusive and extrusive potassic magmatism
724 in SW England. Transactions of the Royal Society of Edinburgh: Earth Sciences 77,
725 349-360.
726 Le Gall, B., Authemayou, C., Ehrhold, A., Paquette, J.-L., Bussien, D., Chazot, G., Aouizerat,
727 A., Pastol, Y., 2014. LiDAR offshore structural mapping and U/Pb zircon/monazite
728 dating of Variscan strain in the Leon metamorphic domain, NW Brittany.
729 Tectonophysics 630, 236-250.
730 Leutwein, F., Chauris, L., Sonet, J., Zimmermann, J.L., 1969. Études géochronologiques et
731 géotectoniques dans le Nord-Finistère (Massif armoricain). Sciences de la Terre, Nancy
732 XIV, 329-358 (in French).
733 Ludwig, K. R., 2008. User's manual for Isoplot 3.70, a geochronological toolkit for Microsoft
734 Excel. Berkeley Geochronology Center Special Publication 4.
735 Maniar, P.D., Piccoli, P.M., 1989. Tectonic discrimination of granitoids. Geological Society
736 of America Bulletin 101, 635-643.

737 Marcoux, E., Cocherie, A., Ruffet, G., Darboux, J.R., Guerrot, C., 2009. Géochronologie
738 revisitée du dôme du Léon (Massif armoricain, France). Géologie de la France 1, 19-40
739 (in French).
740 Masuda, A., Kawakami, O., Dohmoto, Y., Takenaka, T., 1987. Lanthanide tetrad effects in
741 nature: Two mutually opposite types W and M. Geochemical Journal 21, 199-124.
742 Middlemost, E.A.K., 1989. Iron oxidation ratios, norms and the classification of volcanic
743 rocks. Chemical Geology 77, 19-26.
744 Paquette, J.L., Balé, P., Ballèvre, M., Georget, Y., 1987. Géochronologie et géochimie des
745 éclogites du Léon : nouvelles contraintes sur l'évolution géodynamique du Nord-Ouest
746 du Massif armoricain. Bulletin of Mineralogy 110, 683-696 (in French).
747 Patiño Douce, A.E., 1995. Experimental generation of hybrid silicic melts by reaction of high-
748 Al basalt with metamorphic rocks. Journal of Geophysical Research 100, 15623-15639.
749 Patiño Douce, A.E., 1999. What do experiments tell us about the relative contributions of
750 crust and mantle to the origin of granitic magmas? In: Castro, A., Fernandez, C.,
751 Vigneresse, J.L. (Eds.), Understanding granites. Integrating New and Classical
752 Techniques. Geological Society, London, Special Publication 158, 55-75.
753 Patiño Douce, A.E., Johnston, A.D., 1991. Phase equilibria and melt productivity in the pelitic
754 system: implication for the origin of peraluminous granitoids and aluminous granulites.
755 Contributions to Mineralogy and Petrology 107, 202-218.
756 Peccerillo, A., Taylor, S.R., 1976. Geochemistry of Eocene calc-alkalic volcanic rocks from
757 the Kastamonu area. Northern Turkey. Contribution to Mineralogy and Petrology 58,
758 63-81.
759 Peppard, D.F., Mason, G.W., Lewey, S., 1969. A tetrad effect in the liquid-liquid extraction
760 ordering of lanthanides (III). Journal of Inorganic and Nuclear Chemistry 31, 2271-
761 2272.

762 Pitard, F.F., 1993. Pierre Gy's sampling theory and sampling practice: heterogeneity,
763 sampling correctness, and statistical process control, 2nd ed. CRC Press.
764 Prelević, D., Foley, S.F., Cvetković, V., Romer, R.L., 2004. Origin of minette by mixing of
765 lamproite and dacite magmas in Veliki Majdan, Serbia. Journal of Petrolology 45, 759-
766 792.
767 Ramírez, J.A., Grundvig, S., 2000. Causes of geochemical diversity in peraluminous granitic
768 plutons: the Jálama pluton, Central-Iberian Zone (Spain and Portugal). Lithos 50, 171-
769 190.
770 Révillon, S., Hureau-Mazaudier, D., 2009. Improvements in digestion protocols for trace
771 element and isotope determinations in stream and lake sediment reference materials
772 (JSd-1, JSd-2, JSd-3, JLk-1 and LKSD-1). Geostandards and Geoanalytical Research
773 33, 397-413.
774 Richard, P., Shimizu, N., Allègre, C.J., 1976. 143Nd/146Nd, a natural tracer: an application to
775 oceanic basalts. Earth and Planetary Science Letters 31, 269-278.
776 Rock, N.M.S., 1987. The nature and origin of lamprophyres: an overview, in: Fitton, J.G.,
777 Upton, B.G.J. (Eds.), Alkaline Igneous Rocks. Geological Society Special Publications,
778 30. Geological Society of London, United Kingdom, pp. 191-226.
779 Rock, N.M.S., 1991. Lamprophyres. Blackie and Son Ltd., Glasgow-London, United
780 Kindom, p. 285.
781 Rogers, N.W., Bachinski, S.W., Henderson, P., Parry, S.J., 1982. Origin of potash-rich basic
782 lamprophyres: trace element data from Arizona minettes. Earth and Planetary Science
783 Letters 57, 305-312.
784 Rolet, J., Le Gall, B., Darboux, J.R., Thonon, P., Gravelle, M., 1986. L'évolution
785 géodynamique dévono-carbonifère de l'extrémité occidentale de la chaîne hercynienne

d'Europe sur le transect Armorique-Cornwall. Bulletin de la Société Géologique de France 8, 43-54 (in French).

Rottura, A., Bargossi, G.M., Caggianelli, A., Del Moro, A., Visonà, D., Tranne, C.A., 1998. Origin and significance of the Permian high-K calc-alkalic magmatism in the central-eastern Southern Alps, Italy. Lithos 45, 329-348.

Schulz, B., Krenn, E., Finger, F., Bratz, H., Klemd, R., 2007. Cadomian and Variscan metamorphic events in the Leon Domain (Armorican massif, France): P-T data and EMP monazite dating, in: Linneman, U., Nance, R., Kraft, P. (Eds), The evolution of the Rheic ocean from Avalonian-Cadomian active margin to Alleghenian-Variscan collision. Geological Society of America Special Papers 423, 267-285.

Sláma, J. and 13 other authors. Plešovice zircon – A new natural reference material for U–Pb and Hf isotopic microanalysis. Chemical Geology 249, 1-35.

Streckeisen, A.L., 1976. To each plutonic rock its proper name. Earth Science Reviews 12, 1-33.

Streckeisen, A.L., Le Maitre, R.W., 1979. A chemical approximation to the modal QAPF classification of the igneous rocks. Neues Jahrbuch für Mineralogie, Abhandlungen 136, 169-206.

Sylvester, P.J., 1998. Post-collisional strongly peraluminous granites. Lithos 45, 29-44.

Turpin, L., Cuney, M., Friedrich, M., Bouchez, J.L., Aubertin, M., 1990. Meta-igneous origin of Hercynian peraluminous granites in the NW French Massif Central: implications for crustal history reconstructions. Contributions to Mineralogy and Petrology 118, 13-32.

van Achterberg, E., Ryan, C.G., Jackson, S.E., Griffin, W., 2001. Data reduction software for LA-ICP-MS, in: Sylvester, P. (Ed.), Laser Ablation- ICPMS in the Earth Science: Principles and Applications. Mineralogical Association of Canada, Short Course Series, Ottowa, Ontario, Canada, 29, pp. 239-243.

Villaseca, C., Barbero, L., Rogers, G., 1998. Crustal origin of Hercynian peraluminous granitic batholiths of Central Spain: petrological, geochemical and isotopic (Sr, Nd) constraints. Lithos 43, 55-79.

Wenzel, Th., Mertz, D.F., Oberhänsli, R., Becker, T., Renne, P.R., 1997. Age, geodynamic setting, and mantle enrichment processes of a K-rich intrusion from the Meissen massif (northern Bohemian massif) and implications for related occurrences from the mid-European Hercynian. Geologische Rundschau 86, 556-570.

Whalen, J.B., Frost, C., 2013. The Q-ANOR diagram: a tool for the petrogenetic and tectonomagmatic characterization of granitic suites. Geological Society of America Abstracts with Programs 45, p. 24.

White, W.M., Patchett, J., 1984. Hf-Nd-Sr isotopes and incompatible element abundances in island Arcs: implications for magma origins and crust-mantle evolution. Earth and Planetary Sciences Letters 67, 167-185.

Wright, T.L., Doherty, P.C., 1970. A linear programming and least squares computer method for solving petrologic mixing problems. Geological Society of America Bulletin 81, 1995-2008.

Wyman, D.A., Kerrich, R., 1993. Archean shoshonitic lamprophyres of the Abitibi Subprovince, Canada: petrogenesis, age, and tectonic setting. Journal of Petrology 34, 1067-1109.

Zen, E-an, 1986. Aluminium enrichment in silicate melts by fractional crystallization: Some mineralogic and petrographic constraints. Journal of Petrology 27, 1095-1117.

Figure captions

Fig. 1. Geological features of the Aber-Ildut/Nord-Ouessant (AI-NO) complex with sample location (black and white dot) and name. (a) Location of the AI-NO complex within the shear-zone patterns in the Armorican Massif. (b) Sketch geological map of the AI-NO complex. Outline of the continental geological formations is from Chauris and Hallégouët (1989) and Chauris (1994). Offshore formations are based on Chauris and Hallégouët (1989) and Le Gall et al. (2014), and modified by taking the new data into account. W-AI: western sector of the Aber-Ildut pluton; E-AI: eastern sector of the Aber-Ildut pluton; NO: North-Ouessant submassif; PGSZ, NASZ, NOSZ: Porspoder-Guissény, North Armorican and North-Ouessant Shear Zone, respectively. (c) Detailed geological map of North-Ouessant. (d) Detailed geological map of the W-AI submassif.

Fig. 2. Q' vs. ANOR diagram for the AI-NO granitoids (Streckeisen and Le Maitre, 1979), considered as a CIPW normative equivalent to the IUGS classification of Streckeisen (1976). The suite trends of Whalen and Frost (2013), corresponding to the four plutonic rock series defined by Frost et al. (2001) in their MALI (modified alkali-lime index) diagram (see Fig. 7b), are also indicated. CIPW norms have been calculated with $Fe_2O_3/FeO = 0.5$ (Middlemost, 1989).

Fig. 3. Triangular $CaO-SiO_2/10-4TiO_2$ plot of Rock (1987), discriminating the whole-rock compositional fields of alkaline and calc-alkalic lamprophyres (AL and CAL, respectively). The AI-NO ultrapotassic dykes are plotted and compared with the compositional fields of AI-NO granitoids and minettes from SW England (Leat et al., 1987). Symbols as in Fig. 2.

858 Fig. 4. U-Pb geochronologic results of the AI monzogranite 13DB05, all given with errors at
859 1 sigma level (ellipses and error bars): a) Concordia diagram with the resultant age (grey
860 ellipse and framed age); b) weighted average $^{206}Pb/^{238}U$ age.
861
862 Fig. 5. Photographs and photomicrographs of various types of rocks from the AI-NO
863 complex. (a) Ovoid granodioritic enclave in the porphyritic monzogranite (W-AI, Porspoder).
864 (b) Porphyritic monzogranite exhibiting red orthoclase megacrysts (W-AI, Porspoder). (c)
865 Mingling pattern between quartz-monzodiorite and two-mica leucogranite (NO, site OS1, Fig.
866 1c). (d) Dyke of leucominette (W-AI, Porspoder). (e) 1.50 m-thick dyke of alkali-feldspar
867 quartz microsyenite (NO, site OS11, Fig. 1c). (f) Photomicrograph of the tourmaline-
868 leucogranite AI2 (Afs: alkali feldspar; Gt: garnet; Tm: tourmaline; Qz: quartz). (g)
869 Photomicrograph of the leucominette AI33 (Bi: biotite).
870
871 Fig. 6. Discrimination diagrams for biotite in peraluminous granitoids (Abdel-Rahman, 1994)
872 and for biotite and phlogopite in lamprophyres (Rock, 1987). AL: alkaline lamprophyres;
873 CAL: calc-alkalic lamprophyres ; UML: ultramafic lamprophyres; LL : lamproites.
874
875 Fig. 7. Discrimination diagrams based on major elements for the AI-NO granitoids,
876 metasedimentary xenoliths and ultrapotassic dykes. (a) Plot of FeO*/(FeO* + MgO) vs. SiO_2,
877 showing the limit between ferroan and magnesian granitoids (Frost et al., 2001). (b) Plot of
878 $Na_2O + K_2O – CaO$ (modified alkali-lime index, MALI) vs. SiO_2, showing the approximate
879 ranges for the alkali, alkali-calcic, calc-alkalic, and calcic rock series (Frost et al., 2001). (c)
880 Plot of ASI (aluminium saturation index) vs. SiO_2, showing the limit between metaluminous
881 and peraluminous granitoids (solid straight line) and the limit between moderately and
882 strongly peraluminous granitoids (dashed line) (Sylvester, 1998; Frost et al., 2001). (d) K_2O

vs. SiO_2 diagram of Peccerillo and Taylor (1976), showing also the calc-alkalic lamprophyre field of Rock (1987). Symbols as in Figs. 2 and 3.

Fig. 8. Variation of MgO, Al_2O_3, P_2O_5, Ba, Eu, and Y vs. SiO_2 for the AI-NO granitoids, metasedimentary xenoliths and ultrapotassic dykes. The dashed line connects the porphyritic syenogranite AI7, the Afs quartz microsyenite OS11 and the leucominette 13DB07 (see text for explanations). Symbols as in Figs. 2, 3, and 7.

Fig. 9. CI-chondrite normalized trace element patterns of AI-ON rocks (normalization values: Barrat et al., 2012). (a) Moderately peraluminous (MP) granitoids and strongly peraluminous (SP) syenogranites. (b) SP leucogranites, metasedimentary xenoliths and ultrapotassic dykes. Numbers indicate the four sectors appearing in the patterns of the tourmaline-leucogranites AI2 and AI3a, reflecting a tetrad effect (see text).

Fig. 10. (a) ε^t_{Nd} vs. initial $^{87}Sr/^{86}Sr$ isotope diagram showing selected AI-NO data compared with pelites and late-Variscan peraluminous granites from the Spanish Central Region (SCR) (Villaseca et al., 1998). Symbols as in Figs. 2, 3 and 7. (b) ε^t_{Nd} vs. initial $^{87}Sr/^{86}Sr$ isotope diagram showing the fields of meta-sedimentary middle-upper crust and lower crust (data from the French Massif Central: Downes and Duthou, 1988; Turpin et al., 1990). Note that the lower crustal metasediments have lower initial $^{87}Sr/^{86}Sr$ and higher initial ε_{Nd} than the middle-upper ones, probably due to isotopic disequilibrium during deep melting of crustal material (Barbero et al., 1995). Such a model might also explain the isotopic difference between the hornfels AI27 and the migmatite AI11 (Fig. 10a).

907 Fig. 11. Block diagram showing magma emplacement via the PGSZ/NOSZ in the W-AI and
908 NO sectors. Colors as in Fig. 1.
909
910 Fig. 12. Plot of (a) K/Ba and (b) Eu/Eu* vs. $TE_{1,3}$ for the AI-NO rocks (except quartz
911 monzodiorites, granodiorites, metasedimentary xenoliths and ultrapotassic dykes). The
912 parameter $TE_{1,3}$ of Irber (1999), used to quantify the degree of tetrad effect, is developed in
913 Table 1. The common range of continental rocks is from Jahn et al. (2001). Symbols as in Fig.
914 2.
915
916 Fig. 13. Compositions of the AI-NO rocks compared to the fields of two peraluminous granite
917 types and metapelites (field contours drawn according to the data of Patiño Douce, 1999). The
918 solid lines correspond to reaction curves that model melt compositions resulting from
919 hybridization of high-Al olivine tholeiite with metapelite (Patiño Douce, 1995, 1999). LP:
920 low pressure ($P \leq 0.5$ GPa); HP: high pressure ($1.2 \leq P \leq 1.5$ GPa).
921
922 Fig. 14. Geochemical diagrams for post-collisional SP granites, inspired from Sylvester
923 (1998). Symbols as in Figs. 2, 3, and 7. (a) Plot of CaO/Na_2O vs. Al_2O_3/TiO_2 for the AI-NO
924 SP granites, metasedimentary xenoliths and ultrapotassic dykes. The MP data are shown as a
925 field, together with the Sylvester's (1998) SP granites. The solid line correspond to the mixing
926 curve (percentage of mixing indicated) between the average Phenerozoic basalt of Condie
927 (1993) and the 850°C, 1 GPa pelite-derived melt of Patiño Douce and Johnston (1991). (b)
928 Plot of Rb/Ba vs. Rb/Sr for the same samples. The dashed line divides the SP granite field
929 according to the clay content of the source. The Condie's (1993) average Phanerozoic basalt
930 and calculated composition of pelite- and psammite-derived SP granitic melts are also
931 indicated, together with a calculated basalt/pelite-derived melt mixing curve (percentage of

932 mixing marked) (Sylvester, 1998). Note that the AI leucominettes plot very close to the
933 average basalt.
934
935 Fig. 15. Conceptual model for the genesis of post-collisional MP and SP granitoids in a
936 thinned and hot lithosphere in the Variscides. Not to scale. Modified after Sylvester (1998).
937

Table 1. Major and trace element data on whole rock.

Type:	Q-MD / GD			P-MG					P-SG	2M-SG		2M-LG	
Location:	*W-AI*	*W-AI*	*NO*	*W-AI*	*W-AI*	*E-AI*	*NO*	*NO*	*W-AI*	*W-AI*	*W-AI*	*Off sh.*	*W-AI*
Sample:	AI6b	AI28	OS1	AI26	13DB05	AI31	LC3	LC4	AI7	AI17	AI23	C34	AI5
Major elements (wt.%)													
SiO_2	65.04	58.60	59.30	64.55	67.30	69.90	71.75	70.10	71.10	72.28	73.40	73.70	73.40
TiO_2	0.99	1.50	1.45	0.78	0.70	0.52	0.34	0.37	0.30	0.20	0.34	0.28	0.23
Al_2O_3	15.38	17.00	16.60	15.22	16.20	15.40	14.02	14.52	14.90	13.76	14.80	14.10	13.50
$Fe_2O_3^{tot}$	6.11	7.80	6.80	4.79	4.30	3.40	2.10	2.52	2.30	1.64	2.40	2.20	1.49
MnO	0.12	0.10	0.09	0.06	0.07	0.07	0.05	0.53	0.05	0.05	0.03	0.05	0.03
MgO	1.68	2.81	3.68	1.38	1.30	1.00	0.65	0.76	0.58	0.30	0.62	0.54	0.34
CaO	2.37	4.37	3.83	2.72	2.62	2.10	0.83	1.03	1.07	0.85	1.29	0.70	0.75
Na_2O	3.90	3.74	3.23	3.17	3.22	3.58	4.00	4.09	3.19	3.24	2.74	3.03	2.62
K_2O	2.45	2.84	3.48	4.66	4.55	4.19	4.63	4.55	5.50	4.53	5.17	4.69	5.90
P_2O_5	0.36	0.62	0.42	0.30	0.26	0.17	0.17	0.19	0.17	0.22	0.15	0.25	0.24
LOI	1.32	0.75	1.16	0.50	0.76	0.74	1.10	1.14	0.74	0.98	0.88	1.24	0.73
Total	99.72	100.13	100.04	98.12	101.28	101.08	99.64	99.80	99.90	98.04	101.81	100.78	99.24
ASI	1.19	1.03	1.07	1.03	1.10	1.10	1.09	1.09	1.15	1.20	1.21	1.28	1.15
Trace elements (ppm)													
Li	504	167	265	122	131	126	-	-	137	376	81.7	185	122
Be	7.0	6.4	6.3	6.1	6.9	9.1	-	-	5.4	15.2	9.3	14.2	14.0
Rb	273	229	280	210	229	222	-	-	276	307	207	359	252
Cs	19.9	16.1	40.5	10.9	19.4	16.6	-	-	16.1	30.4	11.6	22.1	13.5
Sr	175	356	439	335	316	283	-	-	163	117	162	137	84
Ba	196	407	586	802	715	521	-	-	457	222	426	242	232
Sc	10	13	14	9	9	6	-	-	6	4	5	5	2
V	76.6	119	120	60.9	51.5	38.1	-	-	18.6	10.4	18.3	15.9	9.4
Cr	9	27	67	33	11	25	-	-	19	10	31	13	9
Co	11.3	18.3	24.2	10.1	9.8	6.2	-	-	3.1	2.0	3.6	1.8	1.4
Ni	7.6	19.8	49.4	7.6	8.6	6.2	-	-	3.6	1.5	3.2	1.9	1.6
Cu	1.9	11.7	8.8	7.2	4.5	0.7	-	-	0.5	0.4	8.2	0.5	0.4
Zn	110	128	135	80	76	122	-	-	58	39	47	42	42
Y	24	29	22	21	21	18	-	-	19	13	12	12	10
Zr	212	225	201	144	286	114	-	-	131	69	86	72	90
Hf	5.3	4.5	5.3	3.8	7.1	3.4	-	-	3.9	2.3	2.8	3.2	2.8
Nb	26	34	31	22	21	21	-	-	22	17	11	21	10
Ta	2.0	1.9	2.0	1.4	1.4	1.9	-	-	2.0	3.0	0.8	3.6	1.3
W	10.3	6.8	6.0	9.8	10.8	5.1	-	-	15.2	29.3	18.1	52.0	15.6
Ga	23	23	24	22	24	23	-	-	22	22	20	24	20
Pb	16.8	12.1	11.3	23.8	20.4	21.5	-	-	33.3	34.4	33.5	29.8	30.7
La	68.2	89.4	46.0	67.7	76.8	67.8	-	-	57.8	24.4	34.8	24.8	23.4
Ce	132	173	90.7	137	142	133	-	-	112	47.1	72.5	52.3	51.2
Pr	14.1	18.8	11.6	14.8	14.8	13.3	-	-	11.8	5.3	8.4	6.3	6.1
Nd	50.1	71.2	43.3	54.0	53.1	44.6	-	-	40.4	18.4	30.0	26.8	21.7
Sm	8.5	11.8	8.0	8.8	8.7	6.8	-	-	7.0	3.6	6.2	5.3	5.3
Eu	1.05	1.86	1.82	1.71	1.55	1.26	-	-	0.96	0.56	1.06	0.70	0.50
Gd	6.48	9.09	6.68	6.40	6.51	5.12	-	-	5.35	3.12	4.45	3.60	4.38
Tb	0.89	1.15	0.87	0.82	0.85	0.65	-	-	0.73	0.48	0.58	0.53	0.57
Dy	4.64	5.56	4.41	4.00	4.17	3.31	-	-	3.68	2.57	2.65	2.85	2.50
Ho	0.87	0.99	0.81	0.76	0.77	0.61	-	-	0.67	0.46	0.42	0.51	0.37
Er	2.31	2.58	2.11	1.94	2.07	1.68	-	-	1.72	1.21	0.96	1.44	0.86
Yb	2.04	1.98	1.69	1.59	1.69	1.49	-	-	1.51	1.14	0.71	1.38	0.64
Lu	0.27	0.27	0.23	0.23	0.23	0.21	-	-	0.21	0.15	0.09	0.19	0.08
Th	20.0	14.8	15.3	22.2	20.4	36.6	-	-	25.9	12.4	21.0	15.8	15.8
U	5.4	6.8	8.7	6.9	3.8	12.9	-	-	7.1	5.3	5.9	2.1	5.2
$TE_{1.3}$	0.99	0.97	0.98	0.98	0.97	1.00	-	-	1.01	1.04	1.04	1.00	1.07

Table 1. (*continued*)

Type:	2M-LG			T-LG		µG	µSY	CAL			MIG	HF
Location:	*W-AI*	*E-AI*	*NO*	*W-AI*	*W-AI*	*W-AI*	*NO*	*W-AI*	*W-AI*	*W-AI*	*W-AI*	*W-AI*
Sample:	AI19	AI30	OS4	AI2	AI3a	AI32	OS11	AI33	13DB06	13DB07	AI11	AI27
Major elements (wt.%)												
SiO_2	74.20	73.90	74.07	74.77	76.97	74.96	63.10	55.50	57.30	56.90	65.58	60.10
TiO_2	0.14	0.15	0.15	0.05	0.06	0.12	0.73	1.46	1.37	1.50	0.75	0.89
Al_2O_3	15.00	14.90	13.34	13.19	12.37	13.61	15.30	15.20	15.00	15.30	13.97	17.10
$Fe_2O_3^{tot}$	1.20	1.30	1.32	0.76	0.54	1.06	4.60	6.80	6.70	6.70	6.65	5.80
MnO	0.03	0.03	0.03	0.12	0.02	0.02	0.04	0.08	0.08	0.07	0.15	0.11
MgO	0.29	0.29	0.22	0.03	0.08	0.18	2.26	3.77	3.72	3.82	1.98	1.80
CaO	0.64	0.63	0.45	0.22	0.25	0.37	1.00	5.42	2.7	2.80	0.62	1.41
Na_2O	3.32	3.41	3.11	3.76	3.08	3.06	2.44	2.08	2.58	2.53	2.22	2.35
K_2O	4.91	4.84	4.79	3.96	4.24	4.97	6.65	5.33	6.30	6.30	5.13	8.26
P_2O_5	0.32	0.28	0.37	0.23	0.15	0.33	0.75	1.36	1.31	1.34	0.10	0.20
LOI	1.00	0.99	1.21	1.10	0.85	1.25	2.38	1.94	1.53	1.55	1.41	0.75
Total	101.04	100.72	99.05	98.19	98.61	99.93	99.24	98.94	98.59	98.81	98.56	98.76
ASI	1.30	1.28	1.25	1.25	1.25	1.27	1.26	0.87	1.04	1.06	1.37	1.13
Trace elements (ppm)												
Li	184	194	59.3	93.9	82.8	76.8	169	180	145	147	487	140
Be	7.5	7.9	7.7	2.4	3.9	3.1	12.2	4.4	6.1	6.4	10.7	4.2
Rb	239	291	279	453	345	316	309	223	186	185	416	331
Cs	23.1	19.8	18.3	14.4	17.4	11.4	6.94	20.2	7.66	7.85	36.5	25.6
Sr	79	77	60	11	33	52	327	2500	2490	2430	74	169
Ba	186	184	156	13	42	136	2380	5310	5690	5620	407	521
Sc	4	3	4	8	2	3	11	15	16	17	13	14
V	6.4	6.0	4.1	0.3	2.6	3.4	82.0	122	128	127	104	115
Cr	5	8	14	2	3	13	48	84	85	80	83	81
Co	1.0	1.4	0.7	0.3	0.6	0.6	11.7	19.4	19.2	11.3	10.6	16.3
Ni	1.1	1.2	0.3	0.3	0.1	0.4	30.5	57.9	60.0	51.6	32.4	34.8
Cu	0.9	0.5	3.5	1.0	0.3	2.9	52.3	7.6	6.5	7.0	1.7	35.3
Zn	43	73	50	28	14	49	127	108	144	142	140	101
Y	12	13	12	4	5	10	23	39	48	50	12	29
Zr	51	66	49	17	17	51	286	566	732	727	70	93
Hf	1.8	2.2	2.0	1.3	0.9	2.0	7.0	12.0	13.8	13.8	1.9	2.6
Nb	12	16	16	29	6	16	15	29	36	37	20	20
Ta	1.9	2.2	2.7	4.7	2.5	2.3	0.8	1.3	1.7	1.7	1.8	1.5
W	19.8	22.5	49.2	62.4	25.5	37.3	58.7	19.1	4.8	5.6	21.0	12.2
Ga	20	23	22	35	21	22	21	21	22	22	22	22
Pb	32.5	31.2	30.6	15.7	21.1	22.7	24.2	20.1	37.2	38.3	22.8	40.1
La	10.9	15.0	10.9	2.1	5.5	9.8	60.8	205	237	291	28.4	43.7
Ce	24.0	34.2	23.6	4.2	11.0	21.8	128.9	399	468	543	57.9	99.0
Pr	2.8	3.9	3.0	0.5	1.3	2.7	14.3	47.8	53.2	60.7	6.6	10.8
Nd	10.3	13.9	11.4	1.8	4.1	11.7	55.5	176	194	222	24.2	40.0
Sm	2.5	3.3	2.8	0.7	1.0	3.0	10.4	26.2	28.6	31.1	4.7	8.2
Eu	0.38	0.40	0.31	0.02	0.10	0.32	2.33	6.43	6.47	6.64	0.62	1.40
Gd	2.38	3.02	2.77	0.63	0.91	2.85	7.99	17.56	16.81	17.83	3.88	7.45
Tb	0.43	0.51	0.48	0.13	0.18	0.46	1.00	1.85	1.91	2.02	0.49	1.04
Dy	2.29	2.67	2.38	0.74	1.01	2.30	4.61	7.56	8.60	9.03	2.50	5.42
Ho	0.41	0.43	0.38	0.12	0.17	0.36	0.82	1.25	1.43	1.50	0.44	0.96
Er	1.06	1.03	0.92	0.36	0.47	0.91	2.04	3.04	3.48	3.62	1.11	2.49
Yb	0.91	0.89	0.74	0.55	0.59	0.77	1.67	2.22	2.62	2.74	0.96	2.10
Lu	0.12	0.11	0.09	0.07	0.08	0.10	0.23	0.29	0.36	0.37	0.13	0.28
Th	7.2	9.6	7.5	1.8	2.4	6.6	21.7	29.5	33.6	35.5	9.6	14.0
U	7.9	4.4	4.8	1.0	3.5	12.5	9.3	6.3	6.9	7.3	4.3	2.6
$TE_{1.3}$	1.11	1.14	1.11	1.17	1.17	1.07	0.99	0.95	0.98	0.96	1.00	1.04

W-(E-)AI: West (East) Aber-Ildut; NO: North-Ouessant. Q-MD: quartz monzodiorite; GD: granodiorite; P-MG: porphyroid monzogranite; P-SG: porphyroid syenogranite; 2M-SG : two-mica syenogranite; 2M-LG : two-mica leucogranite; T-LG : tourmaline-leucogranite; µG : two-mica microgranite; µSY : Afs quartz microsyenite; CAL: calc-alkaline lamprophyre (leucominette); MIG: migmatite; HF: hornfels. The aluminum saturation index (ASI) is defined as the molecular ratio Al/(Ca-1.67·P+Na+K) (Frost et al., 2001).
The degree of tetrad effect $TE_{1.3}$ (Irber, 1999) is defined as:

Samples collected during field trips in 2013 and 2014, except LC3 and LC4 (Chauris, 1991) and C34 (Le Gall et al., 2014). Major elements were analyzed by ICP-AES (IUEM, Brest, France) following the analytical method described by Cotten et al. (1995); trace elements were analyzed by ICP-MS (IUEM, Brest, France) following the sample preparation and analysis method of Barrat et al. (1996).

Table 2. Isotopic data on whole rock samples from Aber-Ildut and North-Ouessant.

Type	Sample	Rb (ppm)	Sr (ppm)	$^{87}Rb/^{86}Sr$	$^{87}Sr/^{86}Sr$	±2σ ($x10^{-6}$)	$(^{87}Sr/^{86}Sr)_i$	Sm (ppm)	Nd (ppm)	$^{147}Sm/^{144}Nd$	$^{143}Nd/^{144}Nd$	±2σ ($x10^{-6}$)	ε^t_{Nd}
							(t=304 Ma)						*(t=304 Ma)*
GD	AI6b	273	175	4.53	0.726221	4	0.70661	8.53	50.1	0.1030	0.512363	4	-1.7
P-MG	AI26	210	335	1.82	0.714056	5	0.70620	8.79	54.0	0.0985	0.512294	4	-2.9
2M-LG	C34	359	137	7.62	0.739488	4	0.70654	5.27	26.8	0.1188	0.512253	6	-4.5
2M-LG	AI19	239	79	8.79	0.750405	4	0.71238	2.46	10.3	0.1447	0.512291	4	-4.7
2M-LG	OS4	279	60	13.53	0.770652	4	0.71211	2.83	11.4	0.1504	0.512273	4	-5.3
T-LG	AI3a	345	33	30.74	0.846528	4	0.71355	1.04	4.1	0.1526	0.512332	7	-4.3
µSY	OS11	309	327	2.74	0.717790	5	0.70592	10.44	55.5	0.1137	0.512325	3	-2.5
CAL	AI33	223	2501	0.26	0.706728	4	0.70561	26.24	176	0.0900	0.512350	3	-2.5
MIG	AI11	416	74	16.44	0.780676	3	0.70957	4.65	24.2	0.1162	0.512212	4	-5.2
HF	AI27	331	169	5.69	0.743674	4	0.71907	8.15	40.0	0.1232	0.511874	4	-12.1

GD: granodiorite; P-MG: porphyritic monzogranite; 2M-LG : two-mica leucogranite; T-LG : tourmaline-leucogranite; µSY : Afs quartz microsyénite; CAL: calc-alkaline lamprophyre (leucominette); MIG: migmatite; HF: hornfels. All Sr and Nd isotope ratios are reported at the 2σ confidence level. The Sr isotopic data were determined by thermal ionization mass spectrometry (TIMS) using a Thermo ElectronTM Triton T1 at the IUEM, Brest, France. Nd isotopic data were determined using a Thermo ElectronTM Neptune MC-ICP-MS at Ifremer, Brest, France. Sr isotopic ratios were normalized to the NBS 987 standard ($^{87}Sr/^{86}Sr$ =0.710264) and Nd ratios to JINDI330 standard ($^{143}Nd/^{144}Nd$ = 0.512094). Measured blanks are 3.9 ppb for Sr and 0.198 ppb for Nd. ε^t_{Nd} values have been calculated with the following CHUR values: $^{143}Nd/^{144}Nd$ = 0.512638 and $^{147}Sm/^{144}Nd$ = 0.1967. 304 Ma is used as approximate age of crystallization.

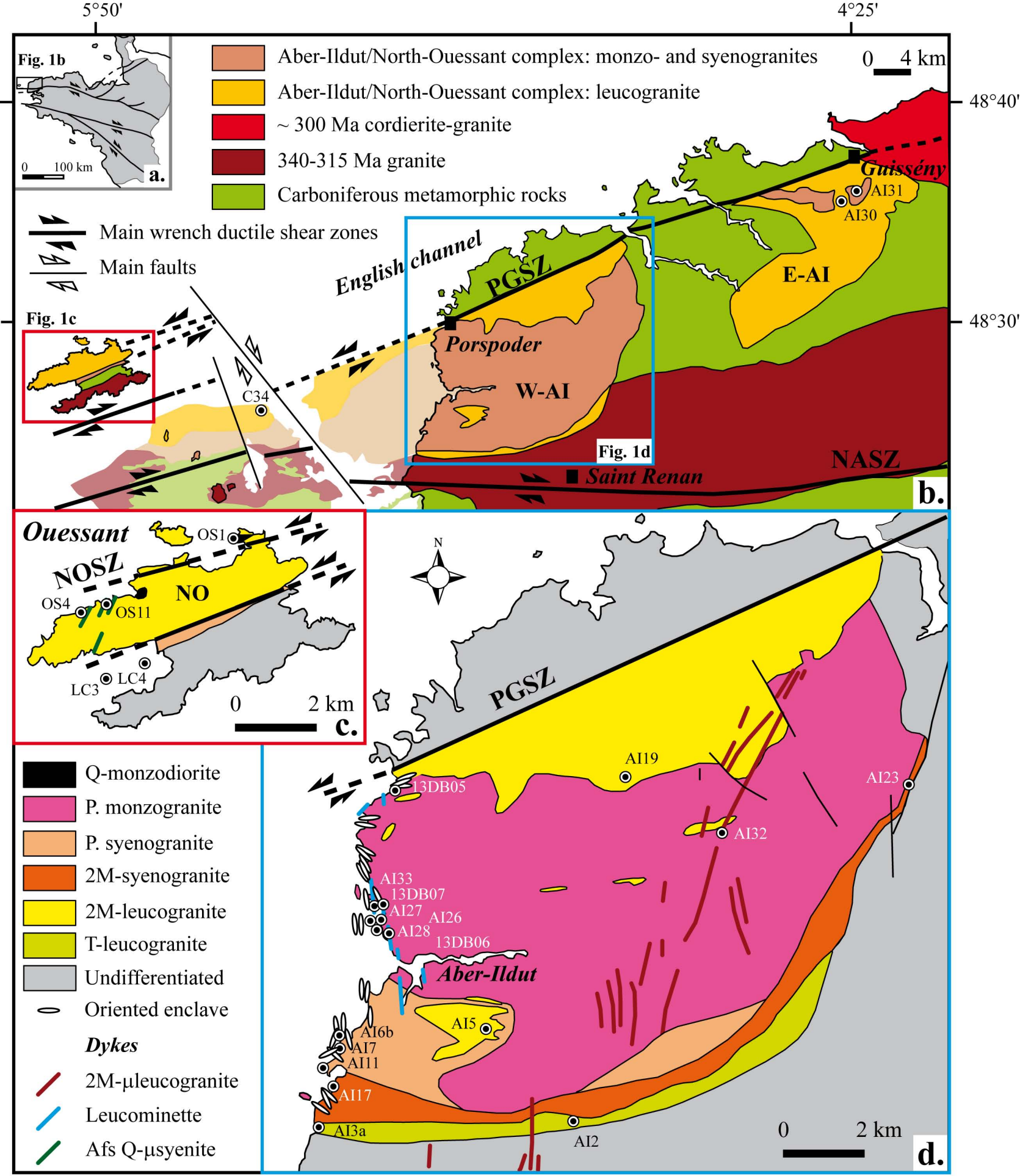
5°50'
4°25'
48°40'
48°30'
Fig. 1b
0 100 km
a.
Aber-Ildut/North-Ouessant complex: monzo- and syenogranites
Aber-Ildut/North-Ouessant complex: leucogranite
~ 300 Ma cordierite-granite
340-315 Ma granite
Carboniferous metamorphic rocks
0 4 km
Main wrench ductile shear zones
Main faults
Fig. 1c
English channel
PGSZ
Guissény
AI31
AI30
E-AI
Porspoder
W-AI
C34
Fig. 1d
NASZ
Saint Renan
b.
Ouessant
OS1
NOSZ
NO
OS4
OS11
LC3
LC4
0 2 km
c.
N
PGSZ
AI19
13DB05
AI23
AI32
AI33
13DB07
AI27
AI26
AI28
13DB06
Aber-Ildut
AI5
AI6b
AI7
AI11
AI17
AI3a
AI2
0 2 km
d.
Q-monzodiorite
P. monzogranite
P. syenogranite
2M-syenogranite
2M-leucogranite
T-leucogranite
Undifferentiated
Oriented enclave
Dykes
2M-µleucogranite
Leucominette
Afs Q-µsyenite

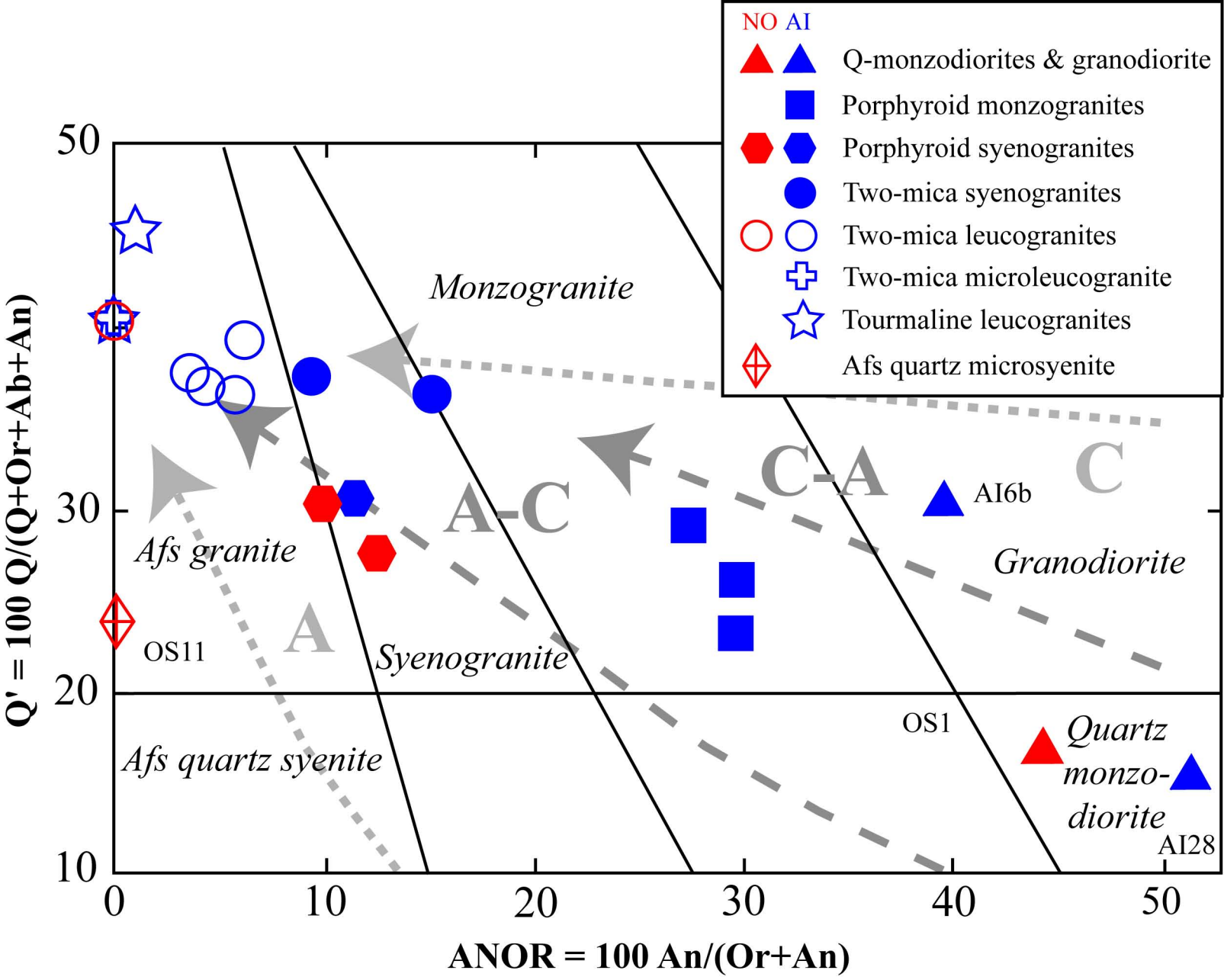
NO AI
Q-monzodiorites & granodiorite
Porphyroid monzogranites
Porphyroid syenogranites
Two-mica syenogranites
Two-mica leucogranites
Two-mica microleucogranite
Tourmaline leucogranites
Afs quartz microsyenite
Monzogranite
Afs granite
A
A-C
C-A
C
Granodiorite
Syenogranite
Afs quartz syenite
Quartz monzo-diorite
OS11
OS1
AI6b
AI28
50
30
20
10
0
10
20
30
40
50
Q' = 100 Q/(Q+Or+Ab+An)
ANOR = 100 An/(Or+An)

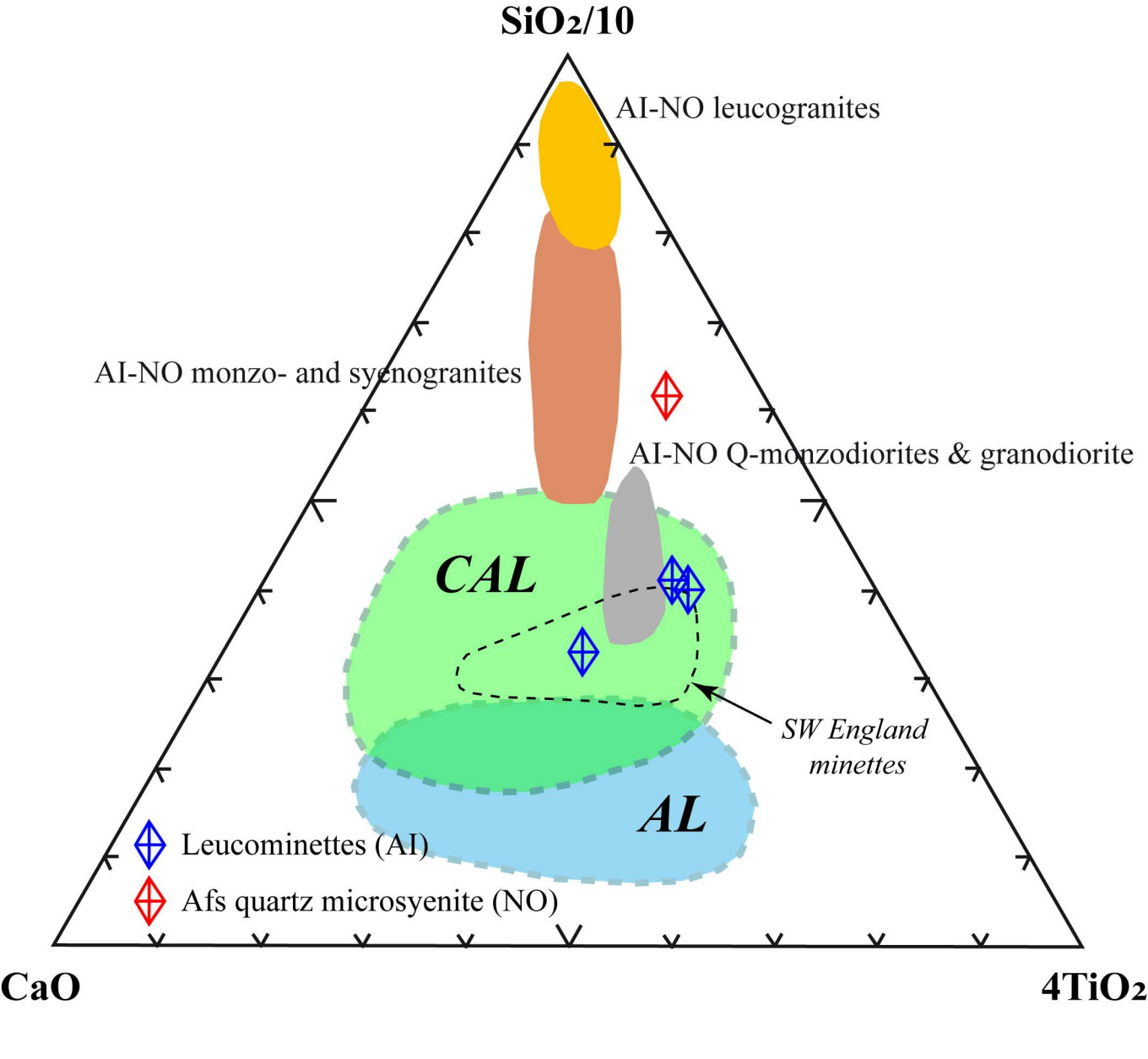
SiO2/10
AI-NO leucogranites
AI-NO monzo- and syenogranites
AI-NO Q-monzodiorites & granodiorite
CAL
AL
SW England
minettes
Leucominettes (AI)
Afs quartz microsyenite (NO)
CaO
4TiO2

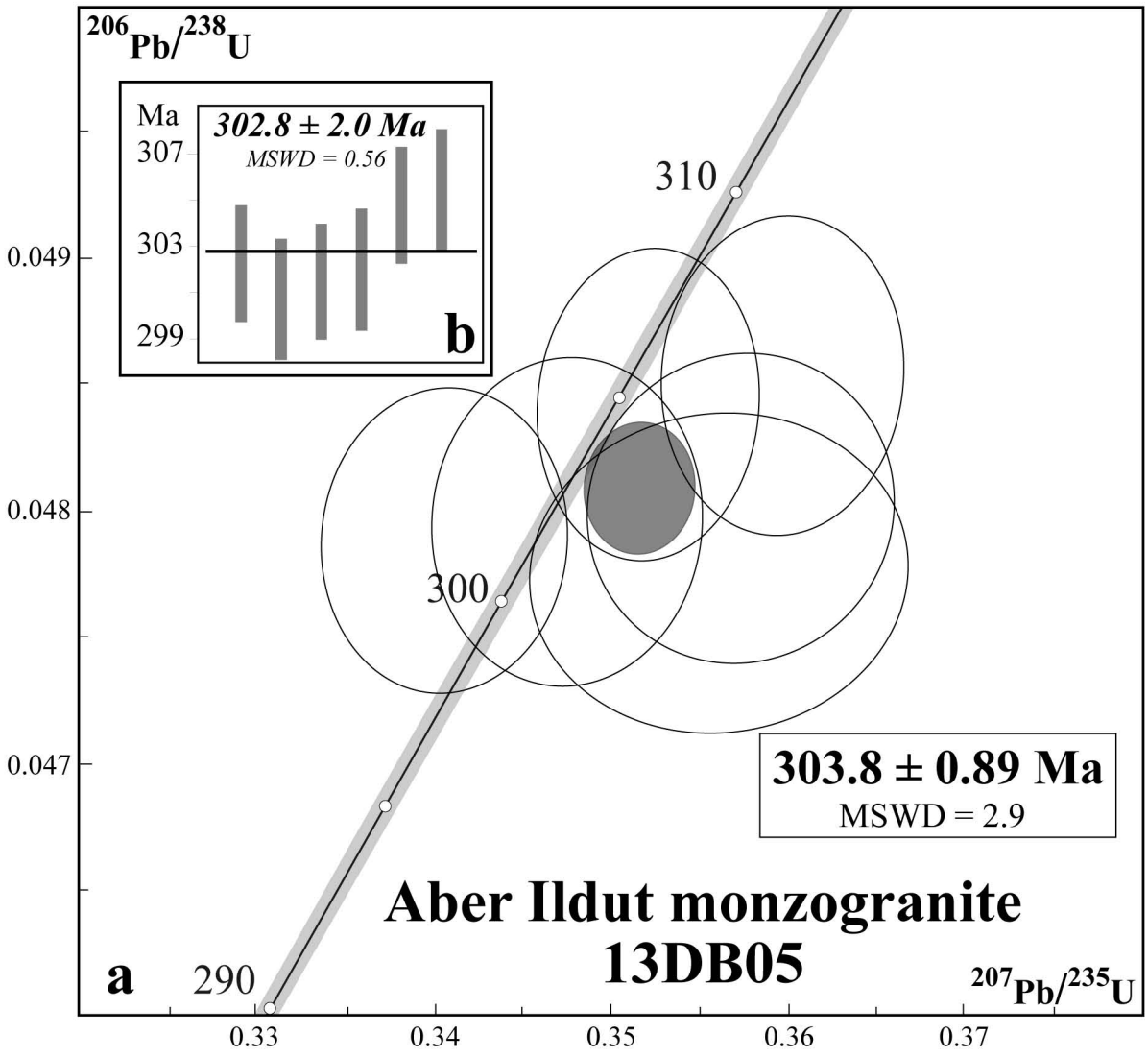
206Pb/238U
Ma
307
303
299
302.8 ± 2.0 Ma
MSWD = 0.56
b
310
300
290
0.049
0.048
0.047
303.8 ± 0.89 Ma
MSWD = 2.9
Aber Ildut monzogranite
13DB05
a
207Pb/235U
0.33
0.34
0.35
0.36
0.37


a.


b.


c.


d.

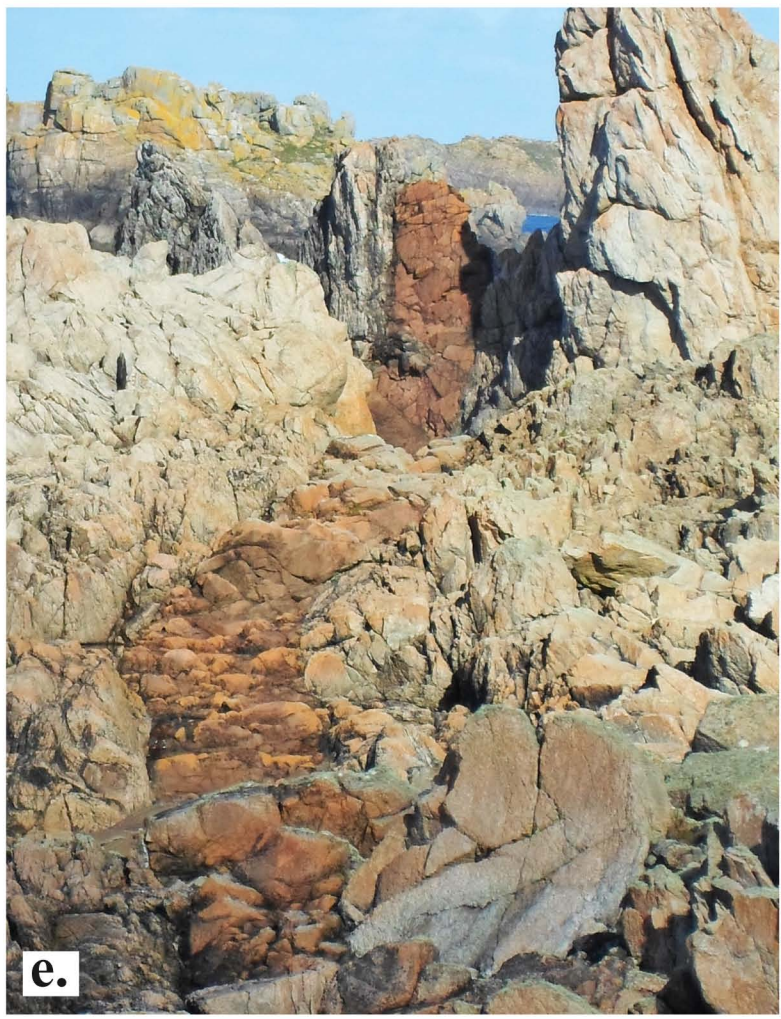
e.

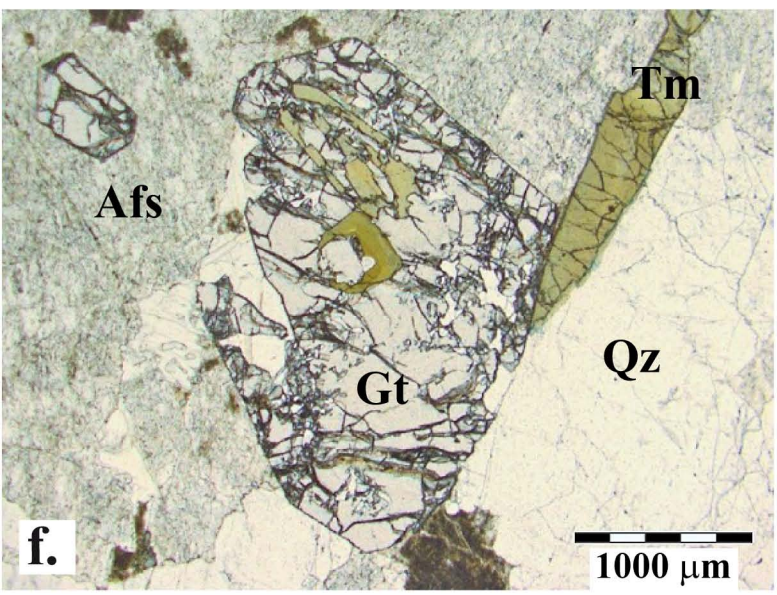
Tm
Afs
Qz
Gt
f.
1000 µm

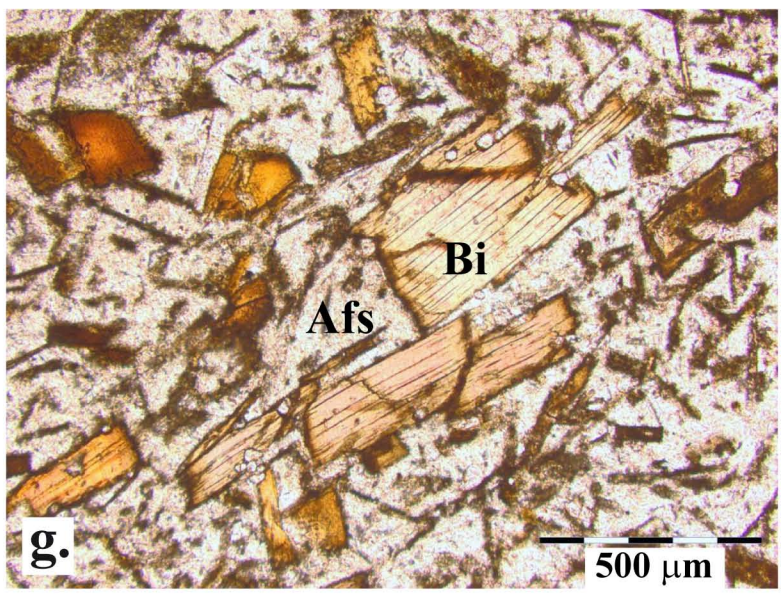
Bi
Afs
g.
500 µm

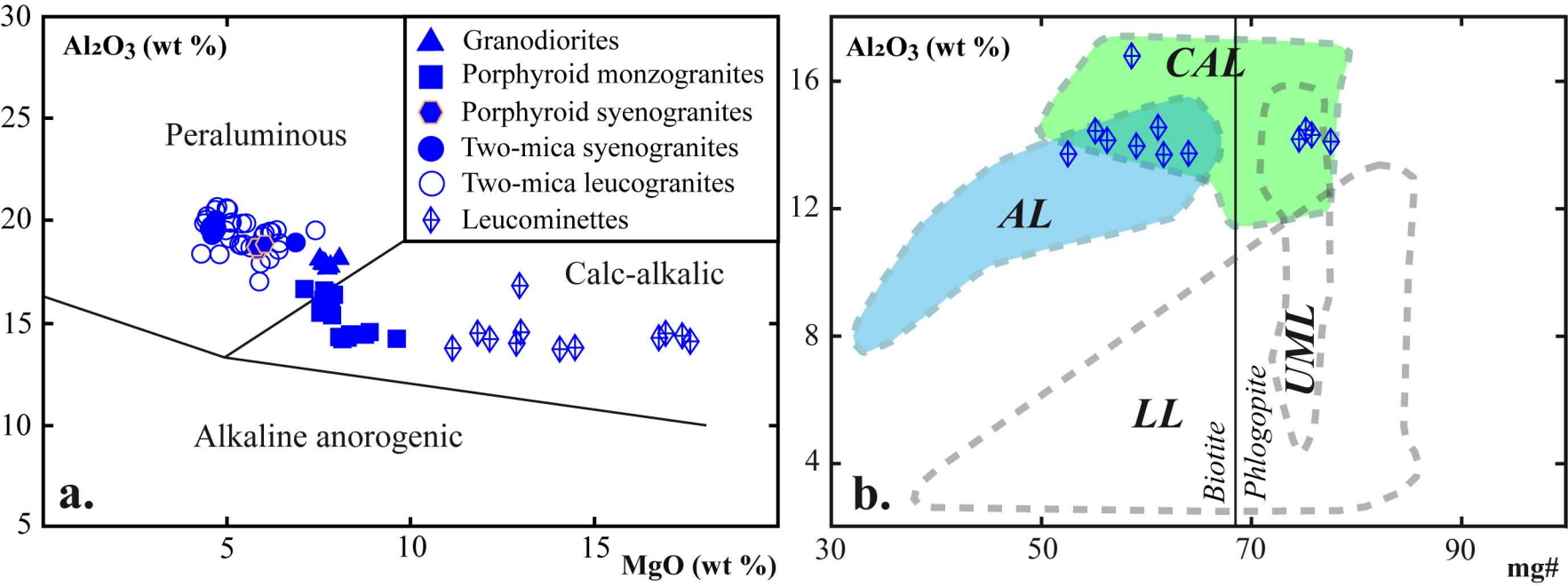
Al2O3 (wt %)
Granodiorites
Porphyroid monzogranites
Porphyroid syenogranites
Two-mica syenogranites
Two-mica leucogranites
Leucominettes
Peraluminous
Calc-alkalic
Alkaline anorogenic
a.
MgO (wt %)
Al2O3 (wt %)
CAL
AL
LL
UML
Biotite
Phlogopite
b.
mg#

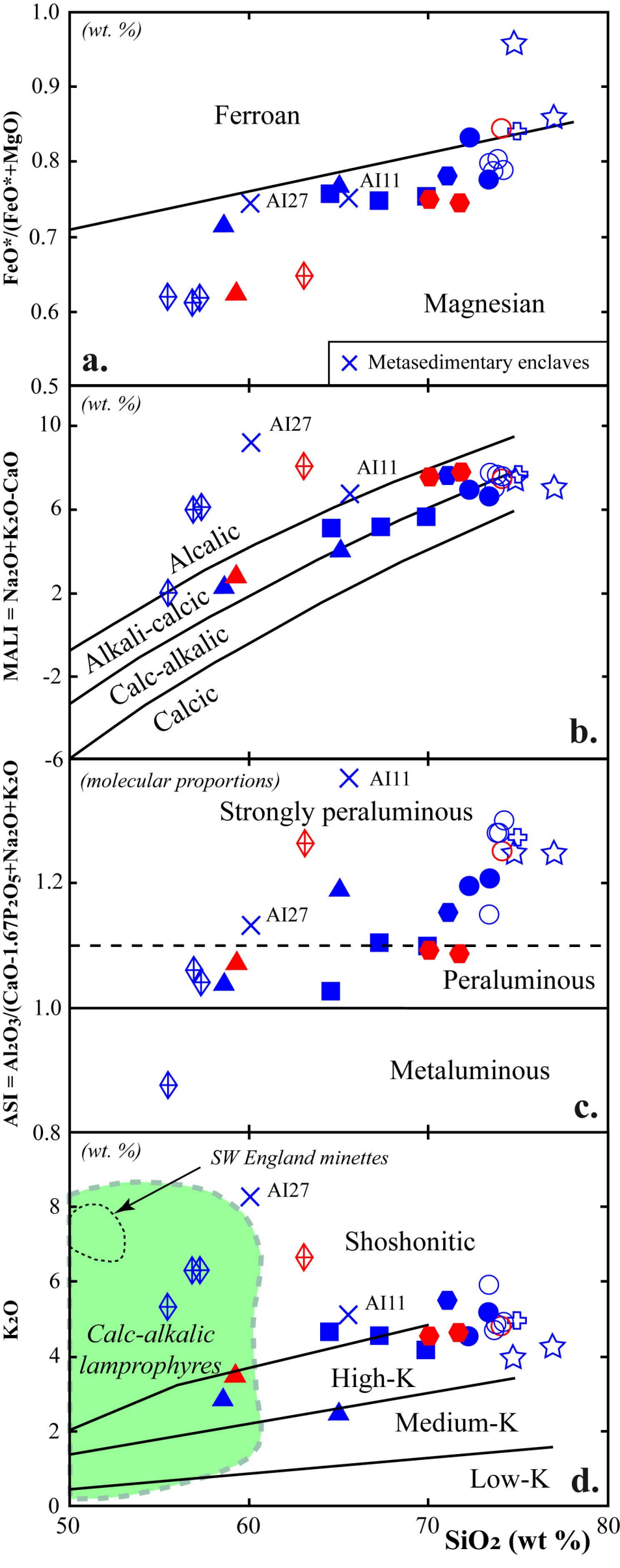
(wt. %)
Ferroan
Magnesian
AI27
AI11
a.
Metasedimentary enclaves
FeO*/(FeO*+MgO)
(wt. %)
AI27
AI11
Alcalic
Alkali-calcic
Calc-alkalic
Calcic
b.
MALI = Na2O+K2O-CaO
(molecular proportions)
AI11
Strongly peraluminous
AI27
Peraluminous
Metaluminous
c.
ASI = Al2O3/(CaO-1.67P2O5+Na2O+K2O
(wt. %)
SW England minettes
AI27
Shoshonitic
AI11
Calc-alkalic
lamprophyres
High-K
Medium-K
Low-K
d.
K2O
SiO2 (wt %)

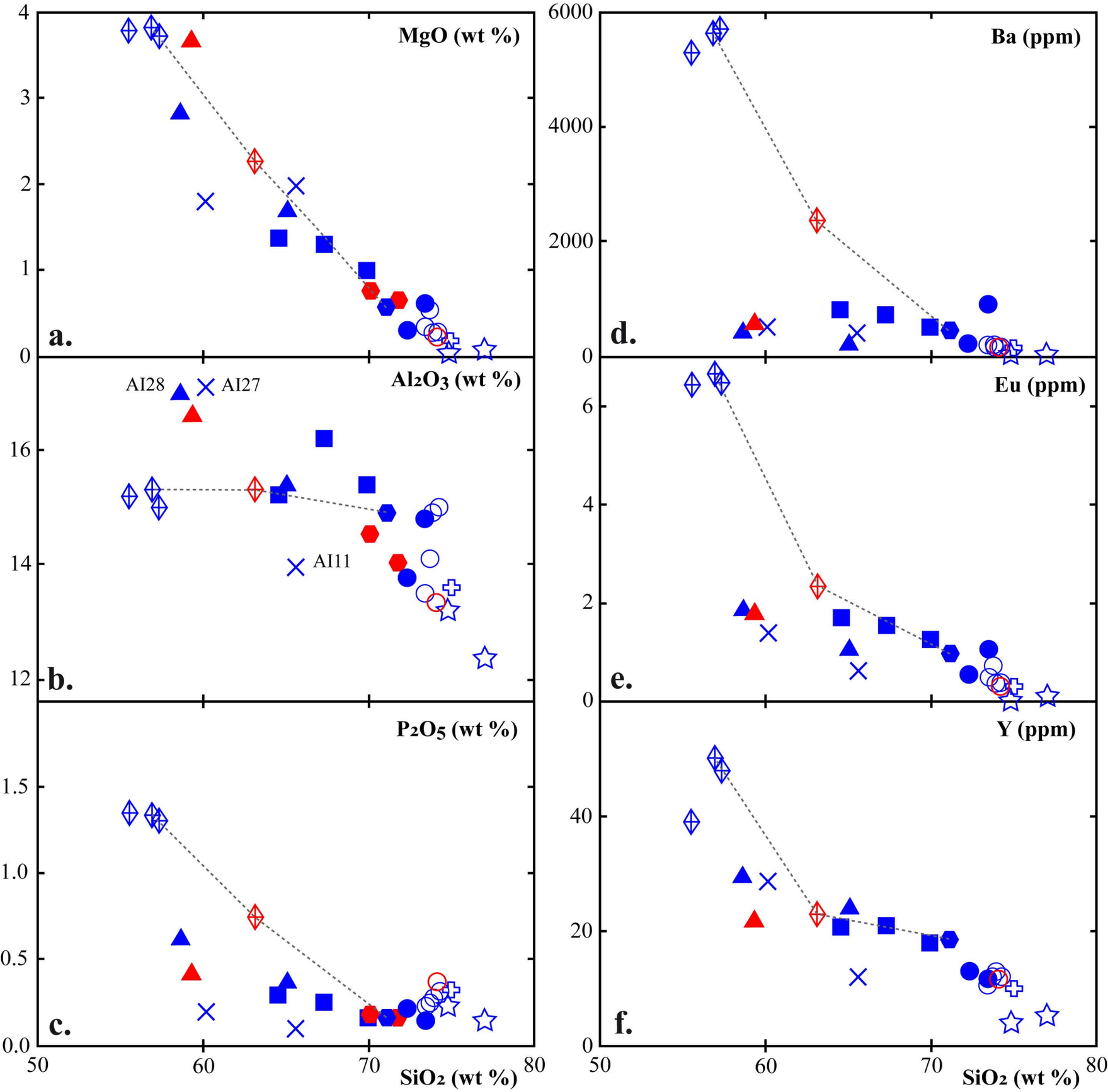
MgO (wt %)
a.
Al2O3 (wt %)
AI28
AI27
AI11
b.
P2O5 (wt %)
c.
Ba (ppm)
d.
Eu (ppm)
e.
Y (ppm)
f.
SiO2 (wt %)
SiO2 (wt %)

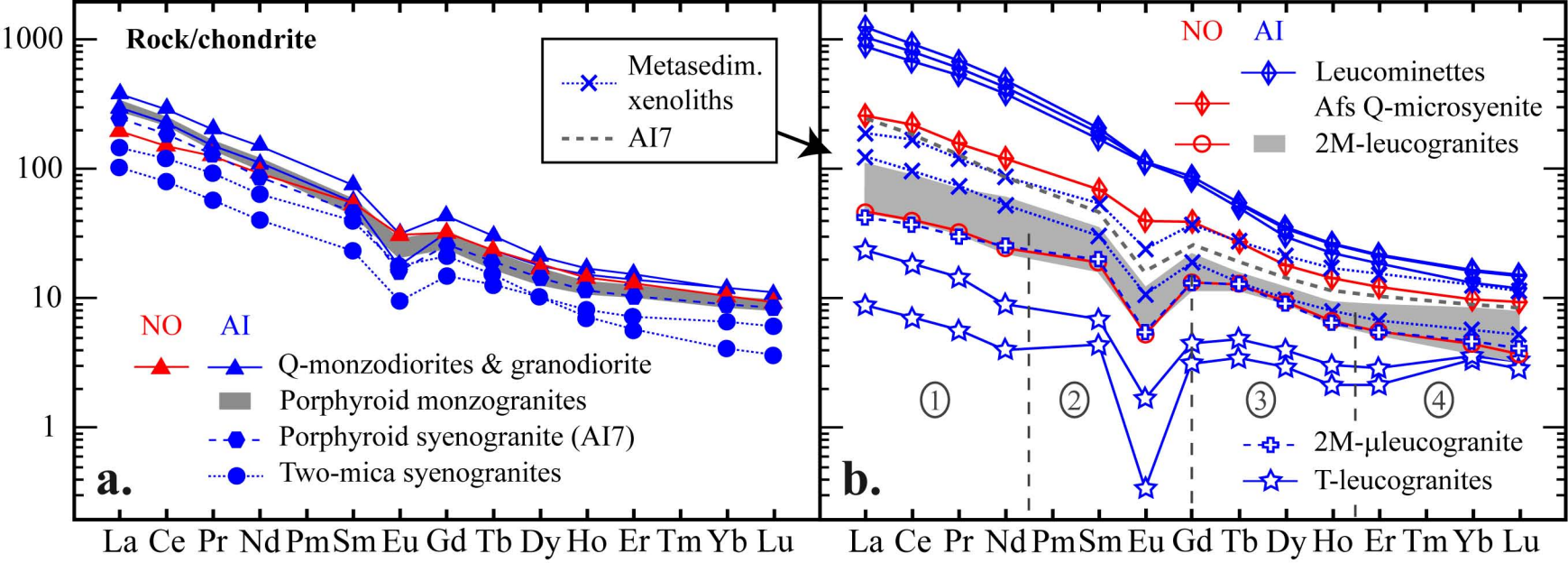
Rock/chondrite
1000
100
10
1
Metasedim. xenoliths
AI7
NO
AI
Q-monzodiorites & granodiorite
Porphyroid monzogranites
Porphyroid syenogranite (AI7)
Two-mica syenogranites
a.
La Ce Pr Nd Pm Sm Eu Gd Tb Dy Ho Er Tm Yb Lu
NO
AI
Leucominettes
Afs Q-microsyenite
2M-leucogranites
①
②
③
④
2M-μleucogranite
T-leucogranites
b.
La Ce Pr Nd Pm Sm Eu Gd Tb Dy Ho Er Tm Yb Lu

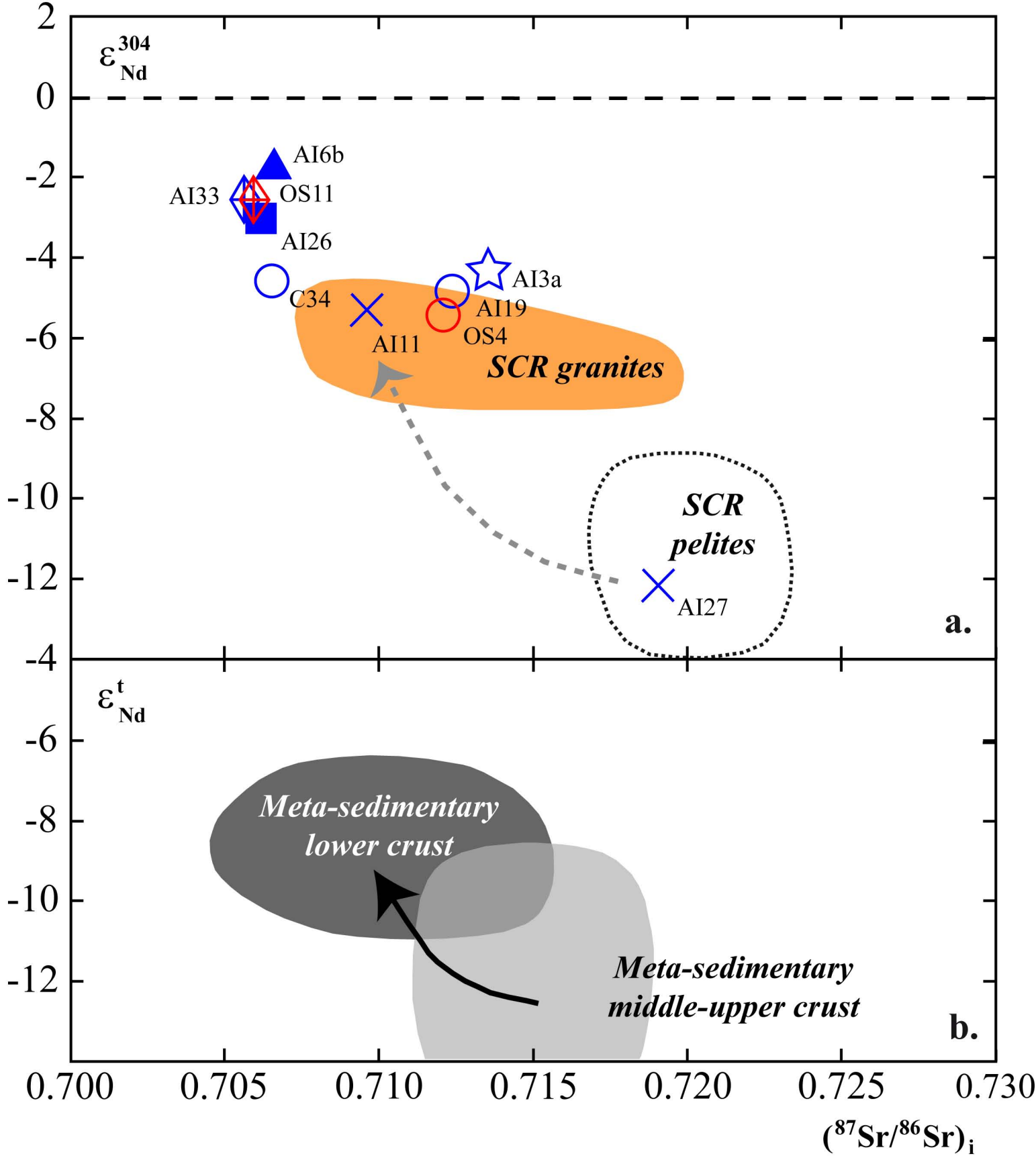
ε^{304}_{Nd}
AI6b
AI33
OS11
AI26
C34
AI3a
AI19
OS4
AI11
SCR granites
SCR pelites
AI27
a.
ε^{t}_{Nd}
Meta-sedimentary lower crust
Meta-sedimentary middle-upper crust
b.
$(^{87}Sr/^{86}Sr)_i$

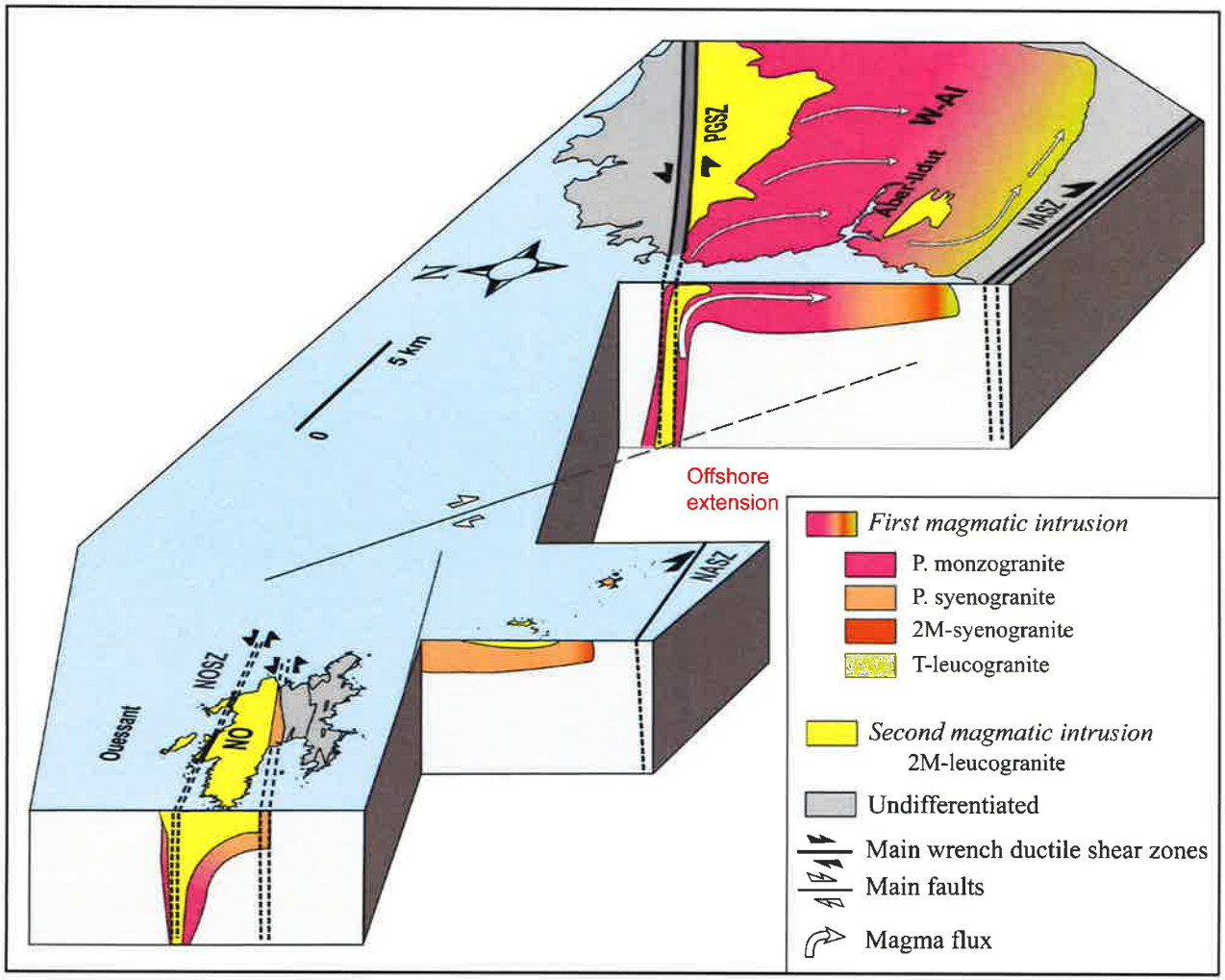
PGSZ
W-Al
Aber-Ildut
NASZ
N
5 km
0
Offshore
extension
NASZ
NOSZ
Ouessant
NO
First magmatic intrusion
P. monzogranite
P. syenogranite
2M-syenogranite
T-leucogranite
Second magmatic intrusion
2M-leucogranite
Undifferentiated
Main wrench ductile shear zones
Main faults
Magma flux

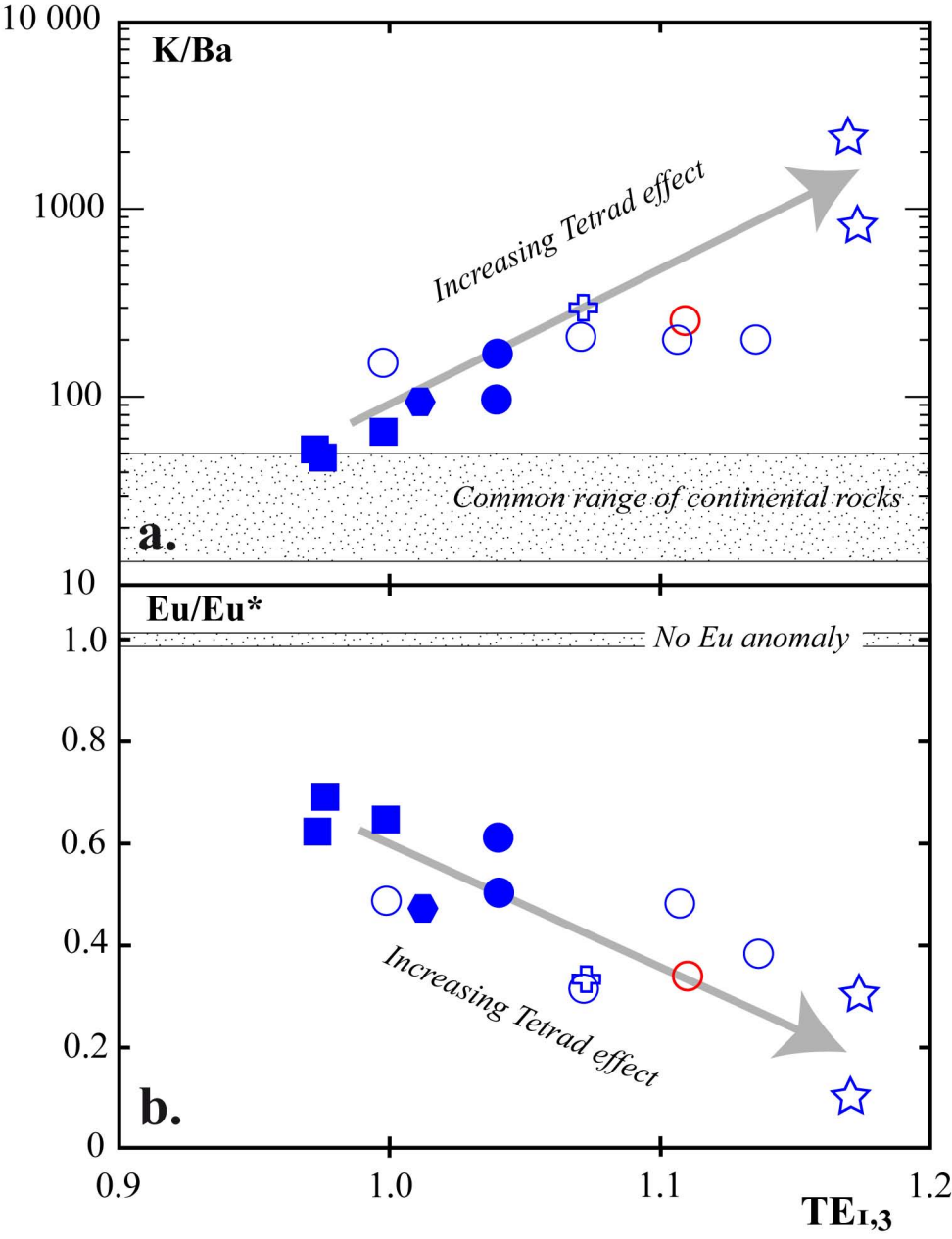
10 000
K/Ba
1000
100
Increasing Tetrad effect
Common range of continental rocks
a.
10
Eu/Eu*
1.0
No Eu anomaly
0.8
0.6
0.4
Increasing Tetrad effect
0.2
b.
0
0.9
1.0
1.1
1.2
TE1,3

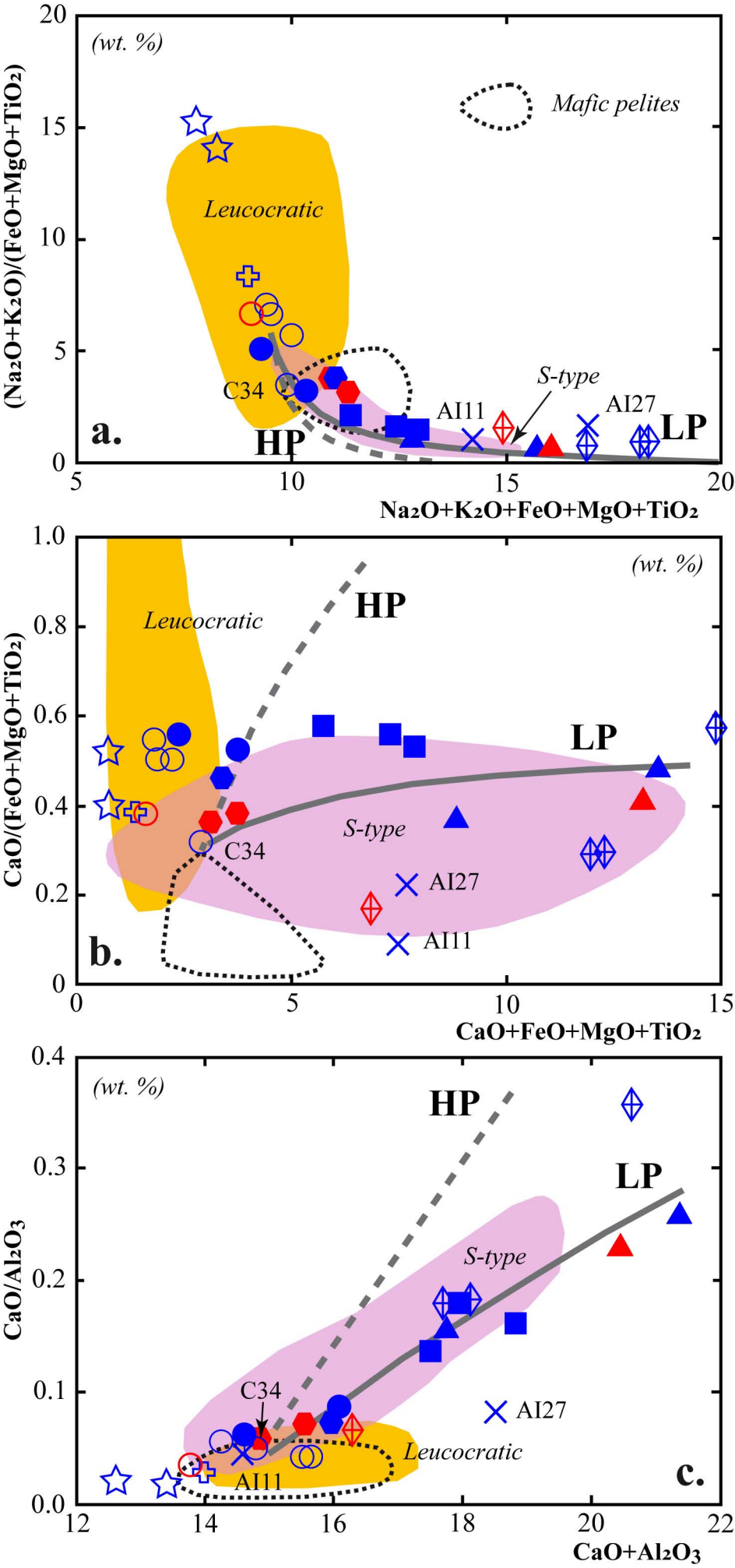
(wt. %)
Mafic pelites
Leucocratic
C34
S-type
AI11
AI27
HP
LP
a.
(Na2O+K2O)/(FeO+MgO+TiO2)
Na2O+K2O+FeO+MgO+TiO2
(wt. %)
HP
Leucocratic
LP
S-type
C34
AI27
AI11
b.
CaO/(FeO+MgO+TiO2)
CaO+FeO+MgO+TiO2
(wt. %)
HP
LP
S-type
C34
AI27
Leucocratic
AI11
c.
CaO/Al2O3
CaO+Al2O3

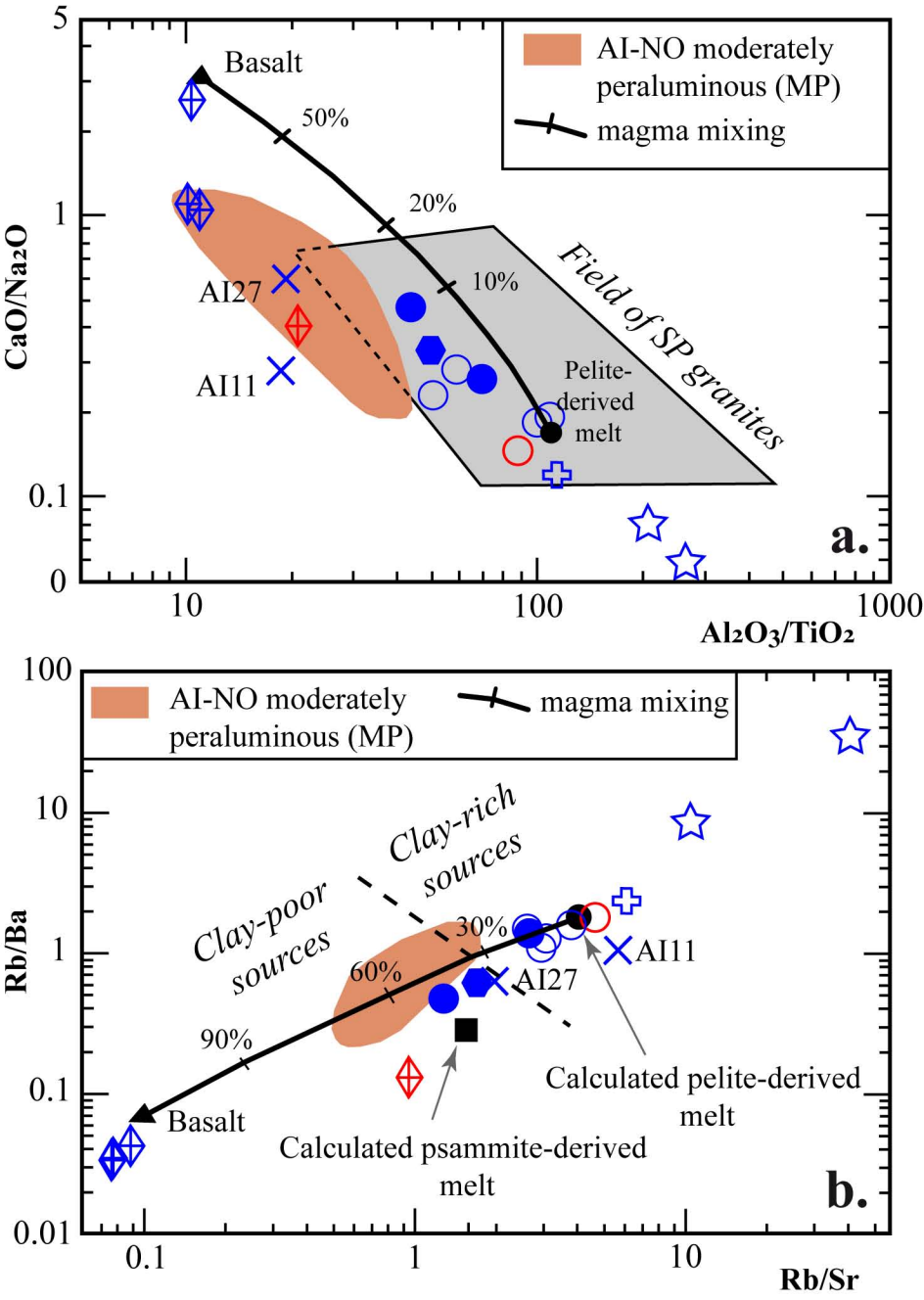
AI-NO moderately peraluminous (MP)
magma mixing
Basalt
50%
20%
10%
Field of SP granites
AI27
AI11
Pelite-derived melt
a.
CaO/Na2O
Al2O3/TiO2
5
1
0.1
0
10
100
1000
AI-NO moderately peraluminous (MP)
magma mixing
Clay-rich sources
Clay-poor sources
30%
60%
90%
AI11
AI27
Basalt
Calculated pelite-derived melt
Calculated psammite-derived melt
b.
Rb/Ba
Rb/Sr
100
10
1
0.1
0.01
0.1
1
10

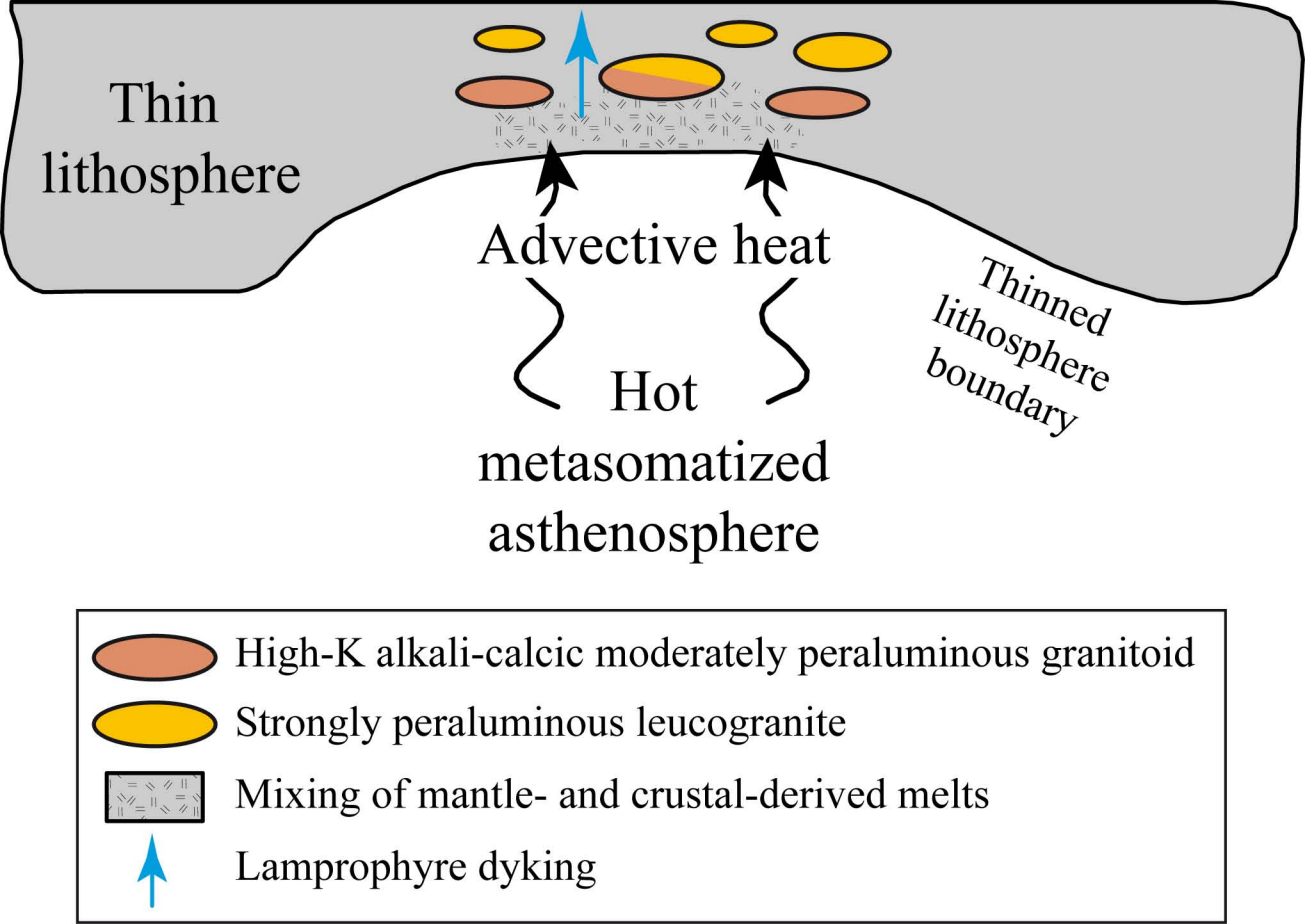
Thin lithosphere
Advective heat
Hot metasomatized asthenosphere
Thinned lithosphere boundary
High-K alkali-calcic moderately peraluminous granitoid
Strongly peraluminous leucogranite
Mixing of mantle- and crustal-derived melts
Lamprophyre dyking